# Including converted waves using Shuey's approximation in elastic full-wavefield migration

Hoogerbrugge, L.; Van Der Neut, J. R.; Van Dongen, K. W.A.; Verschuur, D. J.

**DOI**
10.1093/gji/ggaf247

**Publication date**
2025

**Document Version**
Final published version

**Published in**
Geophysical Journal International

Geophysical Journal International

*Geophys. J. Int.* (2025) **242,** 1–23
Advance Access publication 2025 July 2
General Geophysical Methods

https://doi.org/10.1093/gji/ggaf247

# Including converted waves using Shuey's approximation in elastic full-wavefield migration

L. Hoogerbrugge [1], J. R. van der Neut,[1] K. W. A. van Dongen[1] and D. J. Verschuur[2]

[1] *Department of Imaging Physics, Delft University of Technology, Lorentzweg 1, 2628 CJ, Delft, the Netherlands. E-mail: hoogerbrugge.l.a@gmail.com*
[2] *Department of Geoscience and Engineering, Delft University of Technology, Stevinweg 1, 2628 CN, Delft, the Netherlands*

Accepted 2025 June 26. Received 2025 May 16; in original form 2024 December 23

## SUMMARY

The phenomenon of elastic wave conversions, where acoustic, pressure (*P*-) waves are converted to elastic, shear (*S*-) waves and vice-versa, is commonly disregarded in seismic imaging. This can lead to lower quality images in regions with strong contrasts in elastic parameters. While a number of methods exist that do take wave conversions into account, they either deal with *P* and *S* waves separately, or are prohibitively computationally expensive, as is the case for elastic full-waveform inversion. In this paper an alternative approach to taking converted waves into account is presented by extending full wavefield migration (FWM) to account for wave conversions. FWM is a full-wavefield inversion method based on explicit, convolutional, one-way propagation and reflection operators in the space–frequency domain. By applying these operators recursively, multiscattering data can be modelled. Using these operators, the FWM algorithm aims to reconstruct the reflection properties of the subsurface (i.e. the 'image'). In this paper, the FWM method is extended by accounting for wave conversions due to angle-dependent reflections and transmissions using an extended version of Shuey's approximation. The resulting algorithm is tested on two synthetic models to give a proof of concept. The results of these tests show that the proposed extension can model wave conversions accurately and yields better inversion results than applying conventional, acoustic FWM.

**Key words:** Inverse theory; Numerical approximations and analysis; Numerical modelling.

## 1 INTRODUCTION

Although the earth is an elastic medium in reality, most of the time seismic imaging methods have treated it as an acoustic medium, due to the challenges in true elastic modelling. In doing so, many significant results have been achieved. However, certain wave propagation effects in the earth are neglected by treating it as an acoustic medium. Specifically, acoustic methods disregard wave conversions, where pressure (*P*-) waves are converted to shear (*S*-) waves and vice versa, as well as the propagation of *S*-waves through the medium.

Two areas in seismic imaging where these aforementioned effects play a particular role are areas with large contrasts and areas below the so-called 'gas clouds'. In the presence of large contrasts, such as around salt structures, the amplitudes of the converted waves may become large, which necessitates a method that takes these conversions into account (Alai *et al.* 2021). Gas clouds, by contrast, block the propagation of *P*-waves, but not *S*-waves (Ensley 1984). Therefore, by incorporating the propagation of *S*-waves in the imaging process, higher quality images of structures below these areas may be obtained.

At time of writing, there are two main strategies to take wave conversions into account. The first strategy is to perform migration for *P* and *S* waves separately (Jones & Davison 2014; Alai *et al.* 2022), by changing the velocity profile used. The advantage of these techniques is that they are computationally inexpensive and relatively easy to implement. However, these techniques examine each mode separately, where ideally one would like to examine all modes in an integrated framework. The second strategy is to use a full wavefield technique such as elastic full-waveform inversion (FWI) (Virieux & Operto 2009; Prieux *et al.* 2013), which takes all elastic effects into account at once. The advantage of these techniques is that they are very powerful, and can be used to make very detailed images of the subsurface. However, they are also computationally expensive, and run the risk of getting trapped in local minima if the starting model is far from the ground truth.

In this paper, we present a third approach, which we name elastic FWM. This method is based on an extension of acoustic full-wavefield migration (FWM) to include wave conversions (Berkhout 2014a). This can be seen as an approach in-between the two aforementioned strategies. Acoustic FWM is a migration technique introduced by Berkhout (Berkhout 2014b) and expanded on by others (Staal 2015;

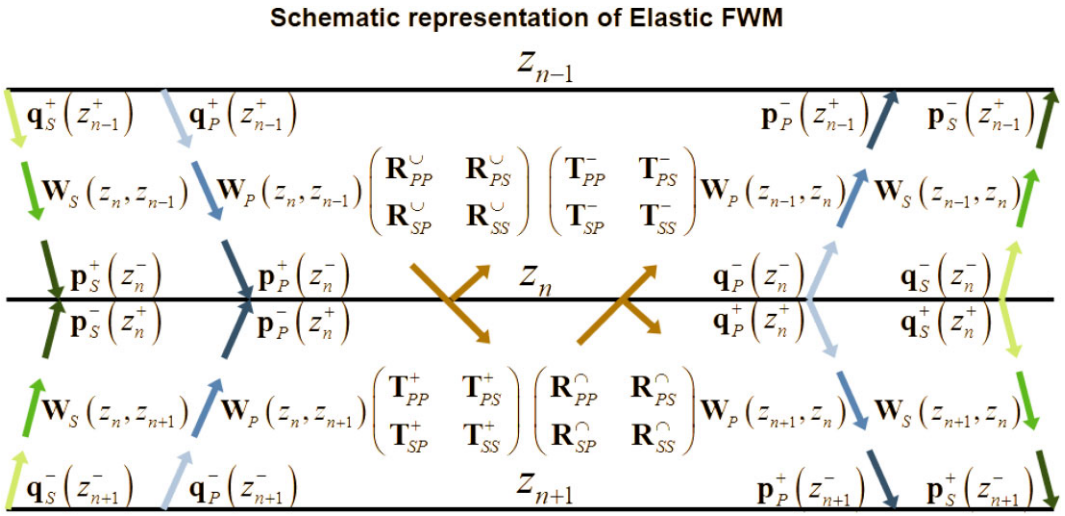


**Figure 1.** Schematic representation of the wavefields and operators at the depth level $z_n$ and the neighbouring levels.

Davydenko & Verschuur 2017; Sun *et al.* 2018). It is based on recursively applying one-way propagation and reflection operators to describe the propagation and scattering of the full wavefield, including all multiples, within the subsurface. It is closely related to the operator-based method developed by Berkhout (2012), which can be seen as the primaries-only version of FWM.

As an elastic migration technique, elastic FWM can be compared to elastic reverse time migration (RTM) (Chang & McMechan 1987; Ren *et al.* 2017), as both rely on a kinematically accurate velocity model to create an image of the subsurface. However, there are two key differences between the methods. First of all, where elastic RTM makes use of two-way wave propagation using finite difference modelling, elastic FWM uses explicit one-way wave propagation operators in the space–frequency domain. This leads to a reduced computational cost (Mulder & Plessix 2004), at the expense of less accurate propagation at large angles. Secondly, as the underlying framework of elastic FWM has been developed specifically to deal with multiple scattering effects, it can naturally describe events which have undergone multiple wave conversions.

The main challenge in extending acoustic FWM to include wave conversion effects is the angle-dependent nature of the elastic transmission and reflection coefficients. Traditionally, angle-dependent reflection and transmission effects are taken into account in FWM by inverting for each angle separately (Davydenko & Verschuur 2017). However, when taking wave conversion effects into account, this approach leads to a significant overparametrization of the reflection and transmission coefficients, as it would require inverting each of the 16 possible reflection and transmission coefficients separately for every angle.

Therefore, to avoid this overparametrization, an extended version of Shuey's approximation is used to link the different reflection and transmission coefficients at all angles (Hoogerbrugge *et al.* 2025). This has the additional benefit of reducing the nonlinearity present in the full elastic reflection and transmission coefficients, making the resulting problem easier to invert. The downside of this approach is that it requires an estimate of the local dip of the reflector to accurately model the wavefield. This estimate can be acquired by first applying a single iteration of acoustic FWM, followed by applying a dip estimation scheme (Fomel 2002).

By combining the extended Shuey's approximations with the extension of the framework of FWM to the elastic case (Berkhout 2014a), we introduce a robust, elastic FWM algorithm which accounts for wave conversions and *S*-wave propagation in a controlled manner. In the remaining four sections of this paper, we present this algorithm in detail. First, the elastic FWM algorithm is described in detail in the Theory section. Next, some preliminary results using this method are presented in the Results section. Some general remarks on the presented method are then discussed in the Discussion section. Finally, the conclusions of this paper are presented in the Conclusions section.

## 2 THEORY

In this section, which consists of four parts, we present the theoretical framework for the extension of 2-D FWM to account for converted waves. First, we examine the extension of the acoustic FWM forward modelling scheme to include converted waves. Next, we examine the propagation operators for *P* and *S* waves in detail. Then, we do the same for the reflection and transmission operators. Finally, we examine the inversion process.

### 2.1 Forward modelling

To include converted waves in the forward modelling algorithm, we follow the structure used by Berkhout (2014a) and begin by examining the wavefields at an interface located at a depth level $z_n$. A schematic representation of this situation is shown in Fig. 1.

At a location right above the interface, which we denote by $\left(x_i, z_n^-\right)$, the $P$-wavefield is given by

$$p_P\left(x_i, z_n^-\right) = p_P^+\left(x_i, z_n^-\right) + q_P^-\left(x_i, z_n^-\right), \tag{1}$$

where we have split the $P$-wavefield $p_P\left(x_i, z_n^-\right)$ into a downgoing component, $p_P^+\left(x_i, z_n^-\right)$, travelling towards the interface and an upgoing component, $q_P^-\left(x_i, z_n^-\right)$, travelling away from the interface. Note that we will work in the Fourier domain throughout this paper, so for example $p_P\left(x_i, z_n^-\right) = p_P\left(x_i, z_n^-, \omega\right)$, with $\omega$ the (angular) frequency.

In a similar way, at a location $\left(x_i, z_n^+\right)$ right below the interface, the $P$-wavefield is given by

$$p_P\left(x_i, z_n^+\right) = p_P^-\left(x_i, z_n^+\right) + q_P^+\left(x_i, z_n^+\right), \tag{2}$$

where we have once again split the $P$-wavefield into an upgoing component, $p_P^-\left(x_i, z_n^+\right)$, travelling towards the interface, and a downgoing component, $q_P^+\left(x_i, z_n^+\right)$, travelling away from the interface.

Repeating the aforementioned process for the $S$-wavefield, we write

$$p_S\left(x_i, z_n^-\right) = p_S^+\left(x_i, z_n^-\right) + q_S^-\left(x_i, z_n^-\right), \tag{3}$$

$$p_S\left(x_i, z_n^+\right) = p_S^-\left(x_i, z_n^+\right) + q_S^+\left(x_i, z_n^+\right). \tag{4}$$

Note the notation used. Superscripts are used to indicate the direction of propagation, where $+$ and $-$ denote downwards and upwards propagation, respectively. The letters $p$ and $q$ are used to denote propagation towards or away from the interface, respectively. Finally, the subscripts $P$ and $S$ are used to differentiate between $P$- and $S$-wavefields, respectively.

We are now interested in the relationship between these different wavefields. As a first step, we assume that our modelling takes place on a rectangular grid, meaning that there are $N_z$ equally spaced depth levels with a spacing of $\Delta z$, and each depth level consists of $N_x$ equally spaced grid points with a spacing of $\Delta x$. We then define a vector $\mathbf{p}_P^+\left(z_n^-\right)$ of length $N_x$, with elements $\mathbf{p}_P^+\left(z_n^-\right)\big|_i = p_P^+\left(x_i, z_n^-\right)$, where the $x_i$'s are the lateral grid points at the depth level $z_n$. In the same way, we define the corresponding vectors for the other wavefield components introduced in eqs (1)–(4).

We now define the relationship between the different wavefield components at a depth level $z_n$. Once again following the formulation used by Berkhout (2014a), we use convolutional reflection and transmission operators, denoted as $\mathbf{R}^{\cap,\cup}_{\cdots}$ and $\mathbf{T}^{\cap,\cup}_{\cdots}$, respectively, to write

$$\begin{pmatrix} \mathbf{q}_P^+\left(z_n^+\right) \\ \mathbf{q}_S^+\left(z_n^+\right) \end{pmatrix} = \begin{pmatrix} \mathbf{R}^{\cap}_{PP} & \mathbf{R}^{\cap}_{PS} \\ \mathbf{R}^{\cap}_{SP} & \mathbf{R}^{\cap}_{SS} \end{pmatrix} \begin{pmatrix} \mathbf{p}_P^-\left(z_n^+\right) \\ \mathbf{p}_S^-\left(z_n^+\right) \end{pmatrix} + \begin{pmatrix} \mathbf{T}^{+}_{PP} & \mathbf{T}^{+}_{PS} \\ \mathbf{T}^{+}_{SP} & \mathbf{T}^{+}_{SS} \end{pmatrix} \begin{pmatrix} \mathbf{p}_P^+\left(z_n^-\right) \\ \mathbf{p}_S^+\left(z_n^-\right) \end{pmatrix}, \tag{5}$$

$$\begin{pmatrix} \mathbf{q}_P^-\left(z_n^-\right) \\ \mathbf{q}_S^-\left(z_n^-\right) \end{pmatrix} = \begin{pmatrix} \mathbf{R}^{\cup}_{PP} & \mathbf{R}^{\cup}_{PS} \\ \mathbf{R}^{\cup}_{SP} & \mathbf{R}^{\cup}_{SS} \end{pmatrix} \begin{pmatrix} \mathbf{p}_P^+\left(z_n^-\right) \\ \mathbf{p}_S^+\left(z_n^-\right) \end{pmatrix} + \begin{pmatrix} \mathbf{T}^{-}_{PP} & \mathbf{T}^{-}_{PS} \\ \mathbf{T}^{-}_{SP} & \mathbf{T}^{-}_{SS} \end{pmatrix} \begin{pmatrix} \mathbf{p}_P^-\left(z_n^+\right) \\ \mathbf{p}_S^-\left(z_n^+\right) \end{pmatrix}, \tag{6}$$

where $\mathbf{R}^{\cap,\cup}_{\cdots}$ and $\mathbf{T}^{\cap,\cup}_{\cdots}$ are matrices of size $N_x \times N_x$ which relate the wavefields above and below the interface. Note that we have dropped the $z_n$-dependence of these matrices for ease of legibility. These operators are described in more detail in Section 2.3. For simplicity, we introduce the following shorthand notation for eqs (5) and (6), viz.

$$\mathbf{q}^+\left(z_n\right) = \mathbf{R}^{\cap}\left(z_n\right)\mathbf{p}^-\left(z_n\right) + \mathbf{T}^{+}\left(z_n\right)\mathbf{p}^+\left(z_n\right), \tag{7}$$

$$\mathbf{q}^-\left(z_n\right) = \mathbf{R}^{\cup}\left(z_n\right)\mathbf{p}^+\left(z_n\right) + \mathbf{T}^{-}\left(z_n\right)\mathbf{p}^-\left(z_n\right), \tag{8}$$

which we will use throughout the rest of this paper.

Next, we examine the relationship between the wavefields at different depth levels $z_n$. To do this, we introduce a set of propagation operators $\mathbf{W}_{P/S}\left(z_{n\pm1}, z_n\right)$ such that

$$\begin{pmatrix} \mathbf{p}_P^+\left(z_{n+1}^-\right) \\ \mathbf{p}_S^+\left(z_{n+1}^-\right) \end{pmatrix} = \begin{pmatrix} \mathbf{W}_P\left(z_{n+1}, z_n\right) & \mathbf{0} \\ \mathbf{0} & \mathbf{W}_S\left(z_{n+1}, z_n\right) \end{pmatrix} \begin{pmatrix} \mathbf{q}_P^+\left(z_n^+\right) \\ \mathbf{q}_S^+\left(z_n^+\right) \end{pmatrix}, \tag{9}$$

$$\begin{pmatrix} \mathbf{p}_P^-\left(z_{n-1}^+\right) \\ \mathbf{p}_S^-\left(z_{n-1}^+\right) \end{pmatrix} = \begin{pmatrix} \mathbf{W}_P\left(z_{n-1}, z_n\right) & \mathbf{0} \\ \mathbf{0} & \mathbf{W}_S\left(z_{n-1}, z_n\right) \end{pmatrix} \begin{pmatrix} \mathbf{q}_P^-\left(z_n^-\right) \\ \mathbf{q}_S^-\left(z_n^-\right) \end{pmatrix}, \tag{10}$$

with $\mathbf{W}_{P/S}\left(z_{n\pm1}, z_n\right)$ matrices of size $N_x \times N_x$ which describe the propagation of waves between the depth levels $z_n$ and $z_{n\pm1}$, and $\mathbf{0}$ the zero matrix of size $N_x \times N_x$. Note that we assume that there is no difference between the propagation of upgoing and downgoing waves between two adjacent depth levels, that is, $\mathbf{W}_{P/S}\left(z_{n+1}, z_n\right) = \mathbf{W}_{P/S}\left(z_n, z_{n+1}\right)$. These operators are described in more detail in Section 2.2. We once again introduce shorthand notation for eqs (9) and (10), viz.

$$\mathbf{p}^+\left(z_{n+1}\right) = \mathbf{W}\left(z_{n+1}, z_n\right)\mathbf{q}^+\left(z_n\right), \tag{11}$$

$$\mathbf{p}^-\left(z_{n-1}\right) = \mathbf{W}\left(z_{n-1}, z_n\right)\mathbf{q}^-\left(z_n\right). \tag{12}$$

With the building blocks of eqs (7), (8), (11) and (12) in place, we now examine the forward modelling algorithm. To initialize the algorithm, we set all upgoing and downgoing wavefields to zero, that is, $\mathbf{p}^{-,0}\left(z_n\right) = \mathbf{p}^{+,0}\left(z_n\right) = \mathbf{0}$. Note the notation of $\mathbf{p}^{-,0}$ and $\mathbf{p}^{+,0}$, where we have introduced an extra number in the superscript, which denotes how many so-called 'round-trips' have been modelled. Each round-trip

increases the maximum order of multiples that are taken into account by one, up to the chosen number of round-trips to be modelled. Furthermore, for simplicity's sake, we assume that there are no sources within the subsurface, only at the surface. Consequently, we set $\mathbf{p}^{+,m}(z_0) = \mathbf{s}_0$ for all $m$ round-trips, where $\mathbf{s}_0$ is a vector containing the source wavefield for one shot at $z = z_0$. Finally, we assume that there are no upgoing waves coming from below the deepest depth level $z_n = z_{N_z}$. Therefore, we write $\mathbf{p}^{-,m}\left(z_{N_z}\right) = \mathbf{0}$ for all $m$ round-trips.

We then begin by computing the downgoing wavefields for the first round-trip. Starting at $z_n = z_0$, we use eq. (7) to write

$$\mathbf{q}^{+,1}(z_0) = \mathbf{T}^{+}(z_0)\,\mathbf{p}^{+,1}(z_0) + \mathbf{R}^{\cap}(z_0)\,\mathbf{p}^{-,0}(z_0)\,. \tag{13}$$

Next, we apply the propagation operators, using eq. (11) to write

$$\mathbf{p}^{+,1}(z_1) = \mathbf{W}(z_1, z_0)\,\mathbf{q}^{+,1}(z_0)\,. \tag{14}$$

At the depth level $z_n = z_1$ we simply repeat this process with the appropriate transmission, reflection and propagation operators. In this way, we model the downgoing wavefield $\mathbf{p}^{+,1}(z_n)$ at all depth levels.

Next, we compute the upgoing wavefield $\mathbf{p}^{-,1}(z_n)$ at all depth levels. We start at the deepest depth level $z_n = z_{N_z}$. We then use eq. (8) to write

$$\mathbf{q}^{-,1}\left(z_{N_z}\right) = \mathbf{T}^{-}\left(z_{N_z}\right)\mathbf{p}^{-,1}\left(z_{N_z}\right) + \mathbf{R}^{\cup}\left(z_{N_z}\right)\mathbf{p}^{+,1}\left(z_{N_z}\right), \tag{15}$$

and apply the propagation operators of eq. (12) to write

$$\mathbf{p}^{-,1}\left(z_{N_z-1}\right) = \mathbf{W}\left(z_{N_z-1}, z_{N_z}\right)\mathbf{q}^{-,1}\left(z_{N_z}\right). \tag{16}$$

Once again, we continue to apply these operators to find the upgoing wavefield $\mathbf{p}^{-,1}(z_n)$ at each depth level.

We now repeat this process as many times as we wish to account for higher order scattering, where the scattering order is increased by one after each round-trip. The full process for finding the wavefields $\mathbf{p}^{+,M}(z_n)$ and $\mathbf{p}^{-,M}(z_n)$ for up to $M$ scattering orders is illustrated in algorithm 1.

**Algorithm 1:** Modeling wavefields

**Result:** $\mathbf{p}^{+,M}(z_n)$ and $\mathbf{p}^{-,M}(z_n)$ for all $z_n$.
**Input:** $\mathbf{s}_0$
Set $\mathbf{p}^{-,0}(z_n) = \mathbf{0}$;
**for** $m = 1 : M$ **do**
  Set $\mathbf{p}^{+,m}(z_0) = \mathbf{s}_0$;
  **for** $n = 0 : N_z - 1$ **do**
    $\mathbf{q}^{+,m}(z_n) = \mathbf{T}^{+}(z_n)\,\mathbf{p}^{+,m}(z_n) + \mathbf{R}^{\cap}(z_n)\,\mathbf{p}^{-,m-1}(z_n)$;
    $\mathbf{p}^{+,m}(z_{n+1}) = \mathbf{W}(z_{n+1}, z_n)\,\mathbf{q}^{+,m}(z_n)$;
  **end**
  Set $\mathbf{p}^{-,m}(z_{N_z}) = \mathbf{0}$;
  **for** $n = N_z : 1$ **do**
    $\mathbf{q}^{-,m}(z_n) = \mathbf{T}^{-}(z_n)\,\mathbf{p}^{-,m}(z_n) + \mathbf{R}^{\cup}(z_n)\,\mathbf{p}^{+,m}(z_n)$;
    $\mathbf{p}^{-,m}(z_{n-1}) = \mathbf{W}(z_{n-1}, z_n)\,\mathbf{q}^{-,m}(z_n)$;
  **end**
**end**

### 2.2 Propagation operators

We now examine the propagation operators introduced in eqs (9) and (10) in more detail. To begin, we examine the propagation operators between a depth level $z_n$ and $z_{n+1}$. We initially assume that the $P$-wave velocity $\alpha\left(z_{n+1/2}\right)$ and $S$-wave velocity $\beta\left(z_{n+1/2}\right)$ are laterally homogeneous between $z_n$ and $z_{n+1}$ and only vary between depth levels. In that case, the propagation of the $P$-wavefield between these depth levels is described in the spatial Fourier domain by (Gisolf & Verschuur 2010)

$$\hat{p}_P^{+}\left(k_x, z_{n+1}^{-}\right) = e^{-jk_{z,P}\left(z_{n+1/2}\right)\Delta z}\hat{q}_P^{+}\left(k_x, z_n^{+}\right), \tag{17}$$

where $j^2 = -1$ and $k_{z,P}\left(z_{n+1/2}\right)$ is given by

$$k_{z,P}^2\left(z_{n+1/2}\right) = \omega^2\alpha^{-2}\left(z_{n+1/2}\right) - k_x^2, \tag{18}$$

where $k_x$ is the spatial frequency. Note that $\hat{q}_P^+\left(k_x, z_n^+\right)$ is obtained by taking the spatial Fourier transform of the wavefield, that is,

$$\hat{q}_P^+\left(k_x, z_n^+\right) = \mathcal{F}\left\{q_P^+\left(x, z_n^+\right)\right\} = \int_{-\infty}^{+\infty} q_P^+\left(x, z_n^+\right) e^{jk_x x} \mathrm{d}x. \tag{19}$$

We now wish to write eq. (17) in the spatial domain. Using the inverse Fourier transform and the convolution property of the Fourier transform (Oppenheim *et al.* 1996), we obtain

$$p_P^+\left(x_i, z_{n+1}^-\right) = \int_{-\infty}^{\infty} W_P\left(x_i - x, z_{n+1}, z_n\right) q_P^+\left(x, z_n^+\right) \mathrm{d}x, \tag{20}$$

with $W_P\left(x, z_{n+1}, z_n\right)$ defined as

$$W_P\left(x, z_{n+1}, z_n\right) = \mathcal{F}^{-1}\left\{e^{-jk_{z,P}\left(z_{n+1/2}\right)\Delta z}\right\}. \tag{21}$$

Note that $W_P\left(x, z_{n+1}, z_n\right)$ is an even function with respect to $x$, as $e^{-jk_{z,P}\left(z_{n+1/2}\right)\Delta z}$ is an even function with respect to $k_x$. Therefore, we write

$$W_P\left(x_i - x, z_{n+1}, z_n\right) = W_P\left(x - x_i, z_{n+1}, z_n\right) = \mathcal{F}^{-1}\left\{e^{-jk_{z,P}\left(z_{n+1/2}\right)\Delta z} e^{jk_x x_i}\right\}. \tag{22}$$

We now discretize eq. (20) as follows

$$p_P^+\left(x_i, z_{n+1}^-\right) = \sum_{j=1}^{N_x} W_P\left(x_j - x_i, z_{n+1}, z_n\right) q_P^+\left(x_j, z_n^+\right) \Delta x, \tag{23}$$

where we have used eq. (22). Rewriting eq. (23) using the notation of eq. (9) yields

$$\mathbf{p}_P^+\left(z_{n+1}^-\right) = \mathbf{W}_P\left(z_{n+1}, z_n\right) \mathbf{q}_P^+\left(z_n^+\right), \tag{24}$$

where $\mathbf{W}_P\left(z_{n+1}, z_n\right)$ is a matrix of size $N_x \times N_x$. Combining eqs (23) and (24), we see that the elements of the propagation operator $\mathbf{W}_P\left(z_{n+1}, z_n\right)$ are given by

$$\mathbf{W}_P\left(z_{n+1}, z_n\right)|_{ij} = W_P\left(x_j - x_i, z_{n+1}, z_n\right) \Delta x, \tag{25}$$

with $W_P\left(x_j - x_i, z_{n+1}, z_n\right)$ defined according to eq. (22).

In a similar way, one can construct the $S$-wave propagation operator $\mathbf{W}_S\left(z_{n+1}, z_n\right)$ by replacing the $P$-wave velocity $\alpha\left(z_{n+1/2}\right)$ in eq. (18) with the $S$-wave velocity $\beta\left(z_{n+1/2}\right)$, viz.

$$k_{z,S}^2\left(z_{n+1/2}\right) = \omega^2 \beta^{-2}\left(z_{n+1/2}\right) - k_x^2, \tag{26}$$

and following the same steps as above.

In situations where the $P$- or $S$-wave velocities are not laterally homogeneous, we approximate the propagation operators by using the local velocity $\alpha\left(x_i, z_{n+1/2}\right)$ or $\beta\left(x_i, z_{n+1/2}\right)$. In this case, $k_{z,P/S}\left(z_{n+1/2}\right)$ becomes laterally heterogeneous, that is, $k_{z,P}^2\left(x_i, z_{n+1/2}\right) = \omega^2 \alpha^{-2}\left(x_i, z_{n+1/2}\right) - k_x^2$. Using this heterogeneous $k_{z,P/S}\left(x_i, z_{n+1/2}\right)$, we approximate the laterally heterogeneous propagation operator by extending eq. (22), that is,

$$W_{P/S}\left(x - x_i, z_{n+1}, z_n\right) = \mathcal{F}^{-1}\left\{e^{-jk_{z,P/S}\left(x_i, z_{n+1/2}\right)\Delta z} e^{jk_x x_i}\right\}. \tag{27}$$

This approximation is reasonable under the condition that the lateral variations in the velocity profile are smooth. In situations where this is not the case, alternative forms of the propagation operator can be used (Wapenaar & Grimbergen 1996; Hammad & Verschuur 2018; Li & Liu 2021).

Finally, we note that evanescent waves cannot be handled within this framework. In order to prevent these waves from creating problems within the inversion, we add a spatial filter to remove them. This gives us the final form of eq. (22), viz.

$$W_{P/S}\left(x - x_i, z_{n+1}, z_n\right) = \mathcal{F}^{-1}\left\{e^{-jk_{z,P/S}\left(x_i, z_{n+1/2}\right)\Delta z} e^{jk_x x_i} F_{P/S}\left(k_x, x_i, z_{n+1/2}\right)\right\}, \tag{28}$$

where the spatial filter $F_P\left(k_x, x_i, z_{n+1/2}\right)$ is defined as

$$F_P\left(k_x, x_i, z_{n+1/2}\right) = \begin{cases} 1 & \forall\, |k_x| < \omega \alpha^{-1}\left(x_i, z_{n+1/2}\right) \\ 0 & \text{else} \end{cases}, \tag{29}$$

with a similar definition for $F_S\left(k_x, x_i, z_{n+1/2}\right)$.

### 2.3 Reflection and transmission operators

In a similar way to the previous section, we now examine the reflection and transmission operators introduced in eqs (5) and (6). As discussed in the introduction, we use an extended version of Shuey's approximation (Shuey 1985; Hoogerbrugge *et al.* 2025) to couple the reflection

and transmission coefficients and to reduce the amount of nonlinearity present in the full (Zoeppritz) elastic transmission and reflection coefficients. To start, we assume a flat reflector at the depth level $z_n$, and assume the incident $P$-wavefield to be a plane wave, striking the interface at an angle $\theta$. In this case, we can approximate the true $PP$-reflection coefficient by taking a Taylor expansion with respect to the angle $\sin(\theta)$ and the contrasts $c_\alpha$, $c_\beta$ and $c_\rho$. Grouping the terms of this Taylor expansion with respect to the order of the angle $\kappa$ and the total order of the contrasts $\lambda$ we write

$$R^{\cup}_{PP}\left(\sin(\theta), c_\alpha, c_\beta, c_\rho\right) \approx \sum_{\kappa=0}^{K}\sum_{\lambda=0}^{\Lambda}\left(\tilde{R}^{\cup}_{PP}\right)^{\kappa}_{\lambda}\sin^{\kappa}(\theta), \tag{30}$$

with

$$\left(\tilde{R}^{\cup}_{PP}\right)^{\kappa}_{\lambda} = \sum_{m=0}^{\lambda}\sum_{k=0}^{\lambda-m}\frac{1}{\kappa!m!k!(\lambda-k-m)!}\frac{d^{\kappa+\lambda}R^{\cup}_{PP}}{d(\sin(\theta))^{\kappa}dc_\alpha^m dc_\beta^k dc_\rho^{(\lambda-k-m)}}\bigg|_{(\mathbf{0})} c_\alpha^m c_\beta^k c_\rho^{(\lambda-k-m)}, \tag{31}$$

where $R^{\cup}_{PP}$ is the full, Zoeppritz $PP$-reflection coefficient for waves from above (Aki & Richards 2002) and with the dimensionless contrast parameters $c_\alpha$, $c_\beta$ and $c_\rho$ defined as

$$c_\alpha = \frac{\alpha(z_n^+) - \alpha(z_n^-)}{\frac{1}{2}\left[\alpha(z_n^+) + \alpha(z_n^-)\right]},\quad c_\beta = \frac{\beta(z_n^+) - \beta(z_n^-)}{\frac{1}{2}\left[\beta(z_n^+) + \beta(z_n^-)\right]},\quad c_\rho = \frac{\rho(z_n^+) - \rho(z_n^-)}{\frac{1}{2}\left[\rho(z_n^+) + \rho(z_n^-)\right]}, \tag{32}$$

where $z_n^+$ and $z_n^-$ denote depth levels just below and above the interface, respectively. While eq. (31) is difficult to evaluate by hand, it can be straightforwardly evaluated using mathematical software such as Maple. Evaluating the above expression for $N = 2$ and $\Lambda = 1$, for example, we find

$$R^{\cup}_{PP}\left(\sin(\theta), c_\alpha, c_\beta, c_\rho\right) \approx \frac{1}{2}(c_\alpha + c_\rho) + \left(\frac{1}{2}c_\alpha - 2\hat{V}^2(c_\rho + 2c_\beta)\right)\sin^2(\theta), \tag{33}$$

which is just the conventional, 2-term Shuey approximation, written in the notation used in this paper.

If the incoming $P$-wavefield is not a pure plane wave, we use the spatial Fourier transform to decompose the wavefield into plane-wave components. In this domain, the angle of incidence $\theta_n$ is given by

$$\sin(\theta_n) = \frac{\bar{\alpha}(z_n)k_x}{\omega}, \tag{34}$$

where $\bar{\alpha}(z_n) = \frac{1}{2}\left[\alpha(z_n^+) + \alpha(z_n^-)\right]$. Note that the angle of incidence depends on the depth level at which the reflector is located, as indicated by the notation $\theta_n$. Using eqs (30) and (34), we approximate the action of the $PP$-reflection coefficient $R^{\cup}_{PP}$ on the downgoing $P$-wavefield at $z = z_n$ in the $k_x$ domain as

$$R^{\cup}_{PP}(k_x, z_n)\hat{p}^+_P(k_x, z_n) \approx \sum_{\kappa=0}^{K}\sum_{\lambda=0}^{\Lambda}\left(\tilde{R}^{\cup}_{PP}\right)^{\kappa}_{\lambda}\left(\frac{\bar{\alpha}(z_n)}{\omega}\right)^{\kappa}k_x^{\kappa}\hat{p}^+_P(k_x, z_n). \tag{35}$$

We now take the inverse Fourier transform of eq. (35) to find the action of the reflection operator in the space domain. Using the convolution property of the Fourier transform (Oppenheim *et al.* 1996) we write

$$\mathcal{F}^{-1}\left\{R^{\cup}_{PP}(k_x, z_n)\hat{p}^+_P(k_x, z_n)\right\} \approx \sum_{\kappa=0}^{K}\sum_{\lambda=0}^{\Lambda}\left(\tilde{R}^{\cup}_{PP}\right)^{\kappa}_{\lambda}S^{\kappa}_{\theta}(x, z_n) * p^+_P(x, z_n), \tag{36}$$

where $*$ represents a convolution with respect to the spatial coordinate $x$, and where

$$S^{\kappa}_{\theta}(x, z_n) = \mathcal{F}^{-1}\left\{\left(\frac{\bar{\alpha}(z_n)}{\omega}\right)^{\kappa}k_x^{\kappa}\right\}. \tag{37}$$

Following the approach of Section 2.2, we now discretize eq. (36) to find the discretized reflection operator

$$\mathbf{R}^{\cup}_{PP}(z_n)\mathbf{p}^+_P(z_n) \approx \sum_{\kappa=0}^{K}\sum_{\lambda=0}^{\Lambda}\left(\tilde{\mathbf{R}}^{\cup}_{PP}\right)^{\kappa}_{\lambda}(z_n)\mathbf{S}^{\kappa}_{\theta}(z_n)\mathbf{p}^+_P(x, z_n), \tag{38}$$

where the matrices $\mathbf{R}^{\cup}_{PP}(z_n)$, $\left(\tilde{\mathbf{R}}^{\cup}_{PP}\right)^{\kappa}_{\lambda}(z_n)$ and $\mathbf{S}^{\kappa}_{\theta}(z_n)$ are matrices of size $N_x \times N_x$. Using the definition of the convolution, we see that the elements of $\mathbf{S}^{\kappa}_{\theta}(z_n)$ are given by

$$\mathbf{S}^{\kappa}_{\theta}(z_n)\big|_{ij} = (-1)^{\kappa}S^{\kappa}_{\theta}(x_j - x_i, z_n)\Delta x, \tag{39}$$

where we have used that $S^{\kappa}_{\theta}(x_j - x_i, z_n)$ is an even function for even values of $\kappa$ and an odd function for odd values of $\kappa$. Using eq. (31) we write the matrices $\left(\tilde{\mathbf{R}}^{\cup}_{PP}\right)^{\kappa}_{\lambda}$ as

$$\left(\tilde{\mathbf{R}}^{\cup}_{PP}\right)^{\kappa}_{\lambda}(z_n) = \sum_{m=0}^{\lambda}\sum_{k=0}^{\lambda-m}\frac{1}{\kappa!m!k!(\lambda-k-m)!}\frac{d^{\kappa+\lambda}R^{\cup}_{PP}}{d(\sin(\theta))^{\kappa}dc_\alpha^m dc_\beta^k dc_\rho^{(\lambda-k-m)}}\bigg|_{(\mathbf{0})}\mathbf{C}^m_\alpha(z_n)\mathbf{C}^k_\beta(z_n)\mathbf{C}^{(\lambda-k-m)}_\rho(z_n), \tag{40}$$

where the matrices $\mathbf{C}_\alpha(z_n)$, $\mathbf{C}_\beta(z_n)$ and $\mathbf{C}_\rho(z_n)$ are diagonal matrices of size $N_x \times N_x$ with elements

$$\mathbf{C}_{...}(z_n)|_{ij} = c_{...}(x_i, z_n)\,\delta_{ij}. \tag{41}$$

We now expand the approach used above to construct the remaining parts of the reflection and transmission operators. We write the full reflection operator $\mathbf{R}^{\cup}(z_n)$ as

$$\mathbf{R}^{\cup}(z_n) = \begin{pmatrix} \mathbf{R}^{\cup}_{PP} & \mathbf{R}^{\cup}_{PS} \\ \mathbf{R}^{\cup}_{SP} & \mathbf{R}^{\cup}_{SS} \end{pmatrix} \approx \sum_{\kappa=0}^{K}\sum_{\lambda=0}^{\Lambda} \begin{pmatrix} \left(\tilde{\mathbf{R}}^{\cup}_{PP}\right)^{\kappa}_{\lambda}\mathbf{S}^{\kappa}_{\theta} & \left(\tilde{\mathbf{R}}^{\cup}_{PS}\right)^{\kappa}_{\lambda}\mathbf{S}^{\kappa}_{\theta} \\ \left(\tilde{\mathbf{R}}^{\cup}_{SP}\right)^{\kappa}_{\lambda}\mathbf{S}^{\kappa}_{\theta} & \left(\tilde{\mathbf{R}}^{\cup}_{SS}\right)^{\kappa}_{\lambda}\mathbf{S}^{\kappa}_{\theta} \end{pmatrix}, \tag{42}$$

where we have omitted the $z_n$ dependency for ease of legibility. In eq. (42) $\left(\tilde{\mathbf{R}}^{\cup}_{PS}\right)^{\kappa}_{\lambda}$, $\left(\tilde{\mathbf{R}}^{\cup}_{SP}\right)^{\kappa}_{\lambda}$ and $\left(\tilde{\mathbf{R}}^{\cup}_{SS}\right)^{\kappa}_{\lambda}$ are matrices of size $N_x \times N_x$ defined in a similar way as $\left(\tilde{\mathbf{R}}^{\cup}_{PP}\right)^{\kappa}_{\lambda}$, that is,

$$\left(\tilde{\mathbf{R}}^{\cup}_{SP}\right)^{\kappa}_{\lambda}(z_n) = \sum_{m=0}^{\lambda}\sum_{k=0}^{\lambda-m} \frac{1}{\kappa!m!k!(\lambda-k-m)!} \left.\frac{d^{\kappa+\lambda}R^{\cup}_{SP}}{d(\sin(\theta))^{\kappa}dc^{m}_{\alpha}dc^{k}_{\beta}dc^{(\lambda-k-m)}_{\rho}}\right|_{(\mathbf{0})} \mathbf{C}^{m}_{\alpha}(z_n)\,\mathbf{C}^{k}_{\beta}(z_n)\,\mathbf{C}^{(\lambda-k-m)}_{\rho}(z_n). \tag{43}$$

The remaining reflection operator $\mathbf{R}^{\cap}(z_n)$ and the transmission operators $\mathbf{T}^{+}(z_n)$ and $\mathbf{T}^{-}(z_n)$ are defined in an analogous way.

Finally, we consider the case where the reflector is not a flat layer. In this case, we must adjust the angle of incidence $\theta$ to account for the local dip. We assume that the interface can be locally approximated to be a flat plane under an angle $\theta_0$. In that case, we use the trigonometric identities $\sin(\theta+\theta_0) = \sin(\theta)\cos(\theta_0) + \cos(\theta)\sin(\theta_0)$ and $\cos(\theta) = \sqrt{1-\sin^2(\theta)}$ to write

$$\sin^{\kappa'}(\theta+\theta_0) = \left[\sin(\theta)\cos(\theta_0) + \sqrt{1-\sin^2(\theta)}\sin(\theta_0)\right]^{\kappa'}. \tag{44}$$

Taking a Taylor expansion with respect to $\sin(\theta)$ gives

$$\sin^{\kappa'}(\theta+\theta_0) \approx \sum_{\kappa=0}^{K} s^{\kappa'}_{\kappa}(\theta_0)\sin^{\kappa}(\theta), \tag{45}$$

with

$$s^{\kappa'}_{\kappa}(\theta_0) = \frac{1}{\kappa!}\left.\frac{d^{\kappa}\sin^{\kappa'}(\theta+\theta_0)}{d(\sin(\theta))^{\kappa}}\right|_{0}. \tag{46}$$

Combining eqs (45) and (30) we can approximate the true $PP$-reflection coefficient for a dipping reflector by

$$R^{\cup}_{PP}\left(\sin(\theta+\theta_0), c_\alpha, c_\beta, c_\rho\right) \approx \sum_{\kappa'=0}^{K}\sum_{\lambda=0}^{\Lambda}\left(\tilde{R}^{\cup}_{PP}\right)^{\kappa'}_{\lambda}\sin^{\kappa'}(\theta+\theta_0) \approx \sum_{\kappa=0}^{K}\sum_{\kappa'=0}^{K}\sum_{\lambda=0}^{\Lambda}\left(\tilde{R}^{\cup}_{PP}\right)^{\kappa'}_{\lambda} s^{\kappa'}_{\kappa}(\theta_0)\sin^{\kappa}(\theta). \tag{47}$$

Using eq. (47), we can write the $PP$-reflection operator for a dipping reflector as

$$\mathbf{R}^{\cup}_{PP}(z_n) \approx \sum_{\kappa=0}^{K}\sum_{\kappa'=0}^{K}\sum_{\lambda=0}^{\Lambda}\left(\tilde{\mathbf{R}}^{\cup}_{PP}\right)^{\kappa'}_{\lambda}(z_n)\,\mathbf{S}^{\kappa'}_{\kappa}(\theta_0)\,\mathbf{S}^{\kappa}_{\theta}(z_n), \tag{48}$$

where $\mathbf{S}^{\kappa'}_{\kappa}(\theta_0)$ is a diagonal matrix of size $N_x \times N_x$ with elements

$$\left.\mathbf{S}^{\kappa'}_{\kappa}(\theta_0)\right|_{ij} = s^{\kappa'}_{\kappa}(\theta_0(x_i, z_n))\,\delta_{ij}. \tag{49}$$

Note that we assume the local dip of the reflector to be known in eq. (45). In practice, this can be computed by first using a conventional imaging technique, or performing a single iteration of elastic FWM using $\theta_0 = 0$, followed by a local dip estimation scheme, such as the one developed by Fomel (2002).

### 2.4 Inversion process

In this section, we examine the inversion process associated with the forward modelling scheme described earlier. We consider a seismic experiment with $N_S$ sources with a known source wavefield $\mathbf{s}_0(z_0)$, $N_x$ receivers located at the surface and $N_\omega$ measured frequencies. In this case, we define the mismatch between the measured data and the forward modelled wavefields at the surface after $M$ round trips as

$$J_M = \frac{1}{2}\sum_{i=1}^{N_\omega}\sum_{j=1}^{N_S}\left\|\mathbf{e}^{M}\left(z_0, s_j, \omega_i, c_\alpha, c_\beta, c_\rho\right)\right\|^2, \tag{50}$$

where we have defined the residual $\mathbf{e}$ as

$$\mathbf{e}^{M}\left(z_0, s_j, \omega_i, c_\alpha, c_\beta, c_\rho\right) = \mathbf{d}\left(z_0, s_j, \omega_i\right) - \mathbf{p}^{-,M}\left(z_0, s_j, \omega_i, c_\alpha, c_\beta, c_\rho\right), \tag{51}$$

with $\mathbf{d}\left(z_0, s_j, \omega_i\right)$ the known data recorded at the surface and the $L2$-norm $\|\cdot\|^2$ defined as

$$\|\mathbf{p}\|^2 = \sum_{i=1}^{N_x} \left(|p_P(x_i)|^2 + |p_S(x_i)|^2\right). \tag{52}$$

Note that in eq. (50) we have explicitly written the dependence of the forward modelled wavefields $\mathbf{p}^{-,M}$ on the contrasts $c_\alpha$, $c_\beta$ and $c_\rho$, the source $s_j$ and the frequency $\omega_i$.

We now apply a gradient descent scheme with respect to the contrasts $c_\alpha$, $c_\beta$ and $c_\rho$ to minimize the objective function $J_M$. To do this, we must first compute the gradient with respect to the contrast parameters. Using algorithm 1, we write the contribution to the forward modelled wavefields at the surface due to the contrasts at a depth level $z_n$ as

$$\mathbf{p}^{-,M}(z_0; z_n) = \bar{\mathbf{W}}^{-}(z_0, z_n)\left[\mathbf{R}^{\cup}(z_n)\,\mathbf{p}^{+,M}(z_n) + \mathbf{T}^{-}(z_n)\,\mathbf{p}^{-,M}(z_n)\right] + \bar{\mathbf{W}}^{\cup}(z_0, z_n)\left[\mathbf{R}^{\cap}(z_n)\,\mathbf{p}^{-,M}(z_n) + \mathbf{T}^{+}(z_n)\,\mathbf{p}^{+,M}(z_n)\right], \tag{53}$$

where we have introduced the operators $\bar{\mathbf{W}}^{-}(z_0, z_n)$ and $\bar{\mathbf{W}}^{\cup}(z_0, z_n)$. These operators are constructed by applying sequences of propagation, reflection and transmission operators and are defined as

$$\bar{\mathbf{W}}^{-}\left(z_j, z_i\right) = \prod_{m=i-1}^{j+1}\left[\mathbf{W}(z_{m-1}, z_m)\,\mathbf{T}^{-}(z_m)\right]\mathbf{W}(z_{i-1}, z_i) \;\; \forall j < i, \tag{54}$$

$$\bar{\mathbf{W}}^{+}\left(z_j, z_i\right) = \prod_{m=i+1}^{j-1}\left[\mathbf{W}(z_{m+1}, z_m)\,\mathbf{T}^{-}(z_m)\right]\mathbf{W}(z_{i+1}, z_i) \;\; \forall j > i, \tag{55}$$

$$\bar{\mathbf{W}}^{\cup}(z_0, z_n) = \sum_{m=n+1}^{N_z} \bar{\mathbf{W}}^{-}(z_0, z_m)\,\mathbf{R}^{\cup}(z_m)\,\bar{\mathbf{W}}^{+}(z_m, z_n). \tag{56}$$

For simplicities' sake, we will focus on the first term of eq. (53), viz.

$$\mathbf{p}^{-,M}\left(z_0; z_n, R^{\cup}\right) = \bar{\mathbf{W}}^{-}(z_0, z_n)\,\mathbf{R}^{\cup}(z_n)\,\mathbf{p}^{+,M}(z_n). \tag{57}$$

Taking the derivative of $\mathbf{p}^{-,M}$ with respect to the contrast $c_\alpha(x_i, z_n)$ gives

$$\frac{\partial p_P^{-,M}\left(x_j, z_0; z_n, R^{\cup}\right)}{\partial c_\alpha(x_i, z_n)} = \bar{\mathbf{W}}_{PP}^{-}(z_0, z_n)\big|_{ji}\frac{\partial \tilde{q}_P^{-,M}(x_i, z_n)}{\partial c_\alpha(x_i, z_n)} + \bar{\mathbf{W}}_{PS}^{-}(z_0, z_n)\big|_{ji}\frac{\partial \tilde{q}_S^{-,M}(x_i, z_n)}{\partial c_\alpha(x_i, z_n)}, \tag{58}$$

$$\frac{\partial p_S^{-,M}\left(x_j, z_0; z_n, R^{\cup}\right)}{\partial c_\alpha(x_i, z_n)} = \bar{\mathbf{W}}_{SP}^{-}(z_0, z_n)\big|_{ji}\frac{\partial \tilde{q}_P^{-,M}(x_i, z_n)}{\partial c_\alpha(x_i, z_n)} + \bar{\mathbf{W}}_{SS}^{-}(z_0, z_n)\big|_{ji}\frac{\partial \tilde{q}_S^{-,M}(x_i, z_n)}{\partial c_\alpha(x_i, z_n)}, \tag{59}$$

where we have introduced the wavefields $\tilde{\mathbf{q}}^{-,M}(z_n)$, which, based on eq. (8), are defined as $\tilde{\mathbf{q}}^{-,M}(z_n) = \mathbf{R}^{\cup}(z_n)\,\mathbf{p}^{+,M}(z_n)$. Taking the derivative of these wavefields with respect to $c_\alpha(x_i, z_n)$ yields

$$\frac{\partial \tilde{q}_P^{-,M}(x_i, z_n)}{\partial c_\alpha(x_i, z_n)} = \sum_{j=1}^{N_x}\frac{\partial\,\mathbf{R}_{PP}^{\cup}(z_n)\big|_{ij}}{\partial c_\alpha(x_i, z_n)}p_P^{+,M}\left(x_j, z_n\right) + \sum_{j=1}^{N_x}\frac{\partial\,\mathbf{R}_{PS}^{\cup}(z_n)\big|_{ij}}{\partial c_\alpha(x_i, z_n)}p_S^{+,M}\left(x_j, z_n\right), \tag{60}$$

$$\frac{\partial \tilde{q}_S^{-,M}(x_i, z_n)}{\partial c_\alpha(x_i, z_n)} = \sum_{j=1}^{N_x}\frac{\partial\,\mathbf{R}_{SP}^{\cup}(z_n)\big|_{ij}}{\partial c_\alpha(x_i, z_n)}p_P^{+,M}\left(x_j, z_n\right) + \sum_{j=1}^{N_x}\frac{\partial\,\mathbf{R}_{SS}^{\cup}(z_n)\big|_{ij}}{\partial c_\alpha(x_i, z_n)}p_S^{+,M}\left(x_j, z_n\right), \tag{61}$$

where we have used the fact that the contrasts $c_\alpha(x_i, z_n)$ at different locations are independent variables. Finally, note the use of the partial extended propagation operators $\bar{\mathbf{W}}_{PP}^{-}$, $\bar{\mathbf{W}}_{PS}^{-}$, $\bar{\mathbf{W}}_{SP}^{-}$ and $\bar{\mathbf{W}}_{SS}^{-}$ in eq. (58). These are matrices of size $N_x \times N_x$, which are related to the full operator $\bar{\mathbf{W}}^{-}$ in the same way as the partial reflection and transmission operators of eq. (6). We now examine these derivatives in more detail. Using eq. (38), we expand $\frac{\partial\,\mathbf{R}_{PP}^{\cup}(z_n)\big|_{ij}}{\partial c_\alpha(x_i, z_n)}$ as

$$\frac{\partial\,\mathbf{R}_{PP}^{\cup}(z_n)\big|_{ij}}{\partial c_\alpha(x_i, z_n)} \approx \sum_{\kappa=0}^{K}\sum_{\lambda=0}^{\Lambda}\frac{\partial\left(\tilde{\mathbf{R}}_{PP}^{\cup}\right)_\lambda^\kappa(z_n)\big|_{ii}}{\partial c_\alpha(x_i, z_n)}\delta_{ij}\,\mathbf{S}_\theta^\kappa(z_n)\big|_{ij}, \tag{62}$$

with

$$\frac{\partial\left(\tilde{\mathbf{R}}_{PP}^{\cup}\right)_\lambda^\kappa(z_n)\big|_{ii}}{\partial c_\alpha(x_i, z_n)} = \sum_{m=1}^{\lambda}\sum_{k=0}^{\lambda-m}\frac{m}{\kappa!m!k!(\lambda-k-m)!}\left.\frac{d^{\kappa+\lambda}R_{PP}^{\cup}}{d(\sin(\theta))^\kappa dc_\alpha^m dc_\beta^k dc_\rho^{(\lambda-k-m)}}\right|_{(\mathbf{0})} c_\alpha^{m-1}c_\beta^k c_\rho^{(\lambda-k-m)}, \tag{63}$$

where we have omitted the $(x_i, z_n)$ dependence for ease of legibility. In a similar way, we can find the derivatives of the other reflection and transmission operators.

We now examine the derivative of the full objective function with respect to the contrast $c_\alpha(x_i, z_n)$. Combining eqs (50), (53), (58) and (59), and once again limiting our analysis to the first term of eq. (53), yields

$$\frac{\partial J\left(R^{\cup}\right)}{\partial c_\alpha(x_i, z_n)} = -\mathrm{Re}\left(\sum_{j=1}^{N_x} \bar{\mathbf{W}}^{-}_{PP}(z_0, z_n)\big|^{*}_{ji} e^{M}_{P}(x_j) \frac{\partial \tilde{q}^{-,M}_{P}(x_i, z_n)^{*}}{\partial c_\alpha(x_i, z_n)} + \bar{\mathbf{W}}^{-}_{PS}(z_0, z_n)\Big|^{*}_{ji} e^{M}_{P}(x_j) \frac{\partial \tilde{q}^{-,M}_{S}(x_i, z_n)^{*}}{\partial c_\alpha(x_i, z_n)} \right.$$
$$\left. + \bar{\mathbf{W}}^{-}_{SP}(z_0, z_n)\big|^{*}_{ji} e^{M}_{S}(x_j) \frac{\partial \tilde{q}^{-,M}_{P}(x_i, z_n)^{*}}{\partial c_\alpha(x_i, z_n)} + \bar{\mathbf{W}}^{-}_{SS}(z_0, z_n)\big|^{*}_{ji} e^{M}_{S}(x_j) \frac{\partial \tilde{q}^{-,M}_{S}(x_i, z_n)^{*}}{\partial c_\alpha(x_i, z_n)}\right), \tag{64}$$

where we have used the superscript $^*$ to indicate complex conjugation. Note the structure of eq. (64): the terms $\bar{\mathbf{W}}^{-}_{\cdots}(z_0, z_n)\big|^{*}_{ji} e^{M}_{P/S}(x_j)$ represent the back-propagation of the data residual at the surface, while the multiplication with $\frac{\partial \tilde{q}^{-,M}_{S/P}(x_i, z_n)^{*}}{\partial c_\alpha(x_i, z_n)}$ represents the application of the imaging condition at the location $(x_i, z_n)$.

We now consider the update direction for all points $x_i$ at depth level $z_n$. We first define a vector $\Delta\mathbf{c}^{R^{\cup}}_{\alpha}(z_n)$, with elements

$$\Delta\mathbf{c}^{R^{\cup}}_{\alpha}(z_n)\Big|_i = -\frac{\partial J_M\left(R^{\cup}\right)}{\partial c_\alpha(x_i, z_n)}. \tag{65}$$

Using eq. (64), we write the vector $\Delta\mathbf{c}^{R^{\cup}}_{\alpha}(z_n)$ as

$$\Delta\mathbf{c}^{R^{\cup}}_{\alpha}(z_n) = \mathrm{Re}\left[\left(\bar{\mathbf{W}}^{-}_{PP}{}^{H}\mathbf{e}^{M}_{P} + \bar{\mathbf{W}}^{-}_{SP}{}^{H}\mathbf{e}^{M}_{S}\right) \circ \left(\left(\partial_{c_\alpha}\mathbf{R}^{\cup}_{PP}\right)\mathbf{p}^{+,M}_{P} + \left(\partial_{c_\alpha}\mathbf{R}^{\cup}_{PS}\right)\mathbf{p}^{+,M}_{S}\right)^{*}\right.$$
$$\left. + \left(\bar{\mathbf{W}}^{-}_{PS}{}^{H}\mathbf{e}^{M}_{P} + \bar{\mathbf{W}}^{-}_{SS}{}^{H}\mathbf{e}^{M}_{S}\right) \circ \left(\left(\partial_{c_\alpha}\mathbf{R}^{\cup}_{SP}\right)\mathbf{p}^{+,M}_{P} + \left(\partial_{c_\alpha}\mathbf{R}^{\cup}_{SS}\right)\mathbf{p}^{+,M}_{S}\right)^{*}\right], \tag{66}$$

where we have used the symbol $\circ$ to denote element wise multiplication and $H$ to denote the conjugate transpose. Note that we have dropped the dependence on the depth level $z_n$ for ease of legibility. Also note the notation $\partial_{c_\alpha}$ to indicate differentiation with respect to $c_\alpha$, where $\partial_{c_\alpha}\mathbf{R}^{\cup}_{PP}$ is a matrix of size $N_x \times N_x$ with elements

$$\partial_{c_\alpha}\mathbf{R}^{\cup}_{PP}\big|_{ij} = \frac{\partial\,\mathbf{R}^{\cup}_{PP}(z_n)\big|_{ij}}{\partial c_\alpha(x_i, z_n)}. \tag{67}$$

Extending the approach described above to the other terms of eq. (53), we write the full update direction of the contrast $c_\alpha$ as a vector $\Delta\mathbf{c}_\alpha(z_n)$, viz.

$$\Delta\mathbf{c}_\alpha(z_n) = \sum_{\omega}\sum_{s}\left[\Delta\mathbf{c}^{R^{\cup}}_{\alpha}(z_n) + \Delta\mathbf{c}^{R^{\cap}}_{\alpha}(z_n) + \Delta\mathbf{c}^{T^{+}}_{\alpha}(z_n) + \Delta\mathbf{c}^{T^{-}}_{\alpha}(z_n)\right]. \tag{68}$$

Given the update direction of eq. (68), we now examine the amplitude of the update. We again limit our analysis to the first term of eq. (53). Using the fact that $\mathbf{R}^{\cup}$ depends linearly on the contrasts gives

$$\Delta\mathbf{p}^{-,M}\left(R^{\cup}\right) = \bar{\mathbf{W}}^{-}\left(\Delta\mathbf{c}_\alpha \circ \partial_{c_\alpha}\mathbf{R}^{\cup} + \Delta\mathbf{c}_\beta \circ \partial_{c_\beta}\mathbf{R}^{\cup} + \Delta\mathbf{c}_\rho \circ \partial_{c_\rho}\mathbf{R}^{\cup}\right)\mathbf{p}^{+,M}, \tag{69}$$

where we have not written the $z_n$ dependence explicitly for ease of legibility.

Extending eq. (69) to include the other terms of eq. (53), we find

$$\Delta\mathbf{p}^{-,M}(z_0) = \sum_{n=1}^{N_z}\Delta\mathbf{p}^{-,M}\left(z_0; z_n, R^{\cup}\right) + \Delta\mathbf{p}^{-,M}\left(z_0; z_n, R^{\cap}\right) + \Delta\mathbf{p}^{-,M}\left(z_0; z_n, T^{+}\right) + \Delta\mathbf{p}^{-,M}\left(z_0; z_n, T^{-}\right), \tag{70}$$

with $\Delta\mathbf{p}^{-,M}(z_0)$ the total change in the wavefields at the surface due to the change in the contrast parameters at all depth levels. We now take the size of the update as

$$\gamma = \frac{\sum_{\omega}\sum_{s}\mathrm{Re}\left(\Delta\mathbf{p}^{-,M}(z_0)^{*}\cdot\mathbf{e}^{M}\right)}{\sum_{\omega}\sum_{s}\left\|\Delta\mathbf{p}^{-,M}(z_0)\right\|^{2}}, \tag{71}$$

where $\cdot$ denotes the vector inner product. Finally, we update the contrast parameters

$$c^{new}_{\alpha}(x_i, z_n) = c^{old}_{\alpha}(x_i, z_n) + \gamma\,\Delta c_\alpha(x_i, z_n), \tag{72}$$

with similar definitions for the $c_\beta$ and $c_\rho$ terms.

The full procedure used to find the gradient can be implemented in a straightforward manner, shown in algorithm 2, analogous to the procedure for wavefield modelling illustrated in algorithm 1. Explicit expressions for the other terms of eq. (68) are given in appendix A.

**Algorithm 2:** Calculating gradients

**Result:** $\Delta\mathbf{c}_\alpha(z_n)$, $\Delta\mathbf{c}_\beta(z_n)$ and $\Delta\mathbf{c}_\rho(z_n)$ for all $z_n$.
**Input:** $\mathbf{p}^{+,M}(z_n)$ and $\mathbf{p}^{-,M}(z_n)$ for all $z_n$.

Set $\bar{\mathbf{W}}^{-}(z_0, z_1) = \mathbf{W}(z_0, z_1)$;
**for** $n = 1 : N_z - 1$ **do**
  **for** $\mathbf{c} \in \{\mathbf{c}_\alpha, \mathbf{c}_\beta, \mathbf{c}_\rho\}$ **do**
    Calculate $\Delta\mathbf{c}^{R^{\cup}}(z_n)$ and $\Delta\mathbf{c}^{T^{-}}(z_n)$;
    $\Delta\mathbf{c}(z_n) = \Delta\mathbf{c}^{R^{\cup}}(z_n) + \Delta\mathbf{c}^{T^{-}}(z_n)$;
  **end**
  $\bar{\mathbf{W}}^{-}(z_0, z_{n+1}) = \bar{\mathbf{W}}^{-}(z_0, z_n)\,\mathbf{T}^{-}(z_n)\,\mathbf{W}(z_n, z_{n+1})$;
**end**
Set $\bar{\mathbf{W}}^{\cup}(z_0, z_{N_z}) = \mathbf{0}$;
**for** $n = N_z - 1 : 1$ **do**
  $\bar{\mathbf{W}}^{\cup}(z_0, z_n) =$
  $\bar{\mathbf{W}}^{\cup}(z_0, z_{n+1})\,\mathbf{T}^{+}(z_{n+1})\,\mathbf{W}(z_{n+1}, z_n) + \bar{\mathbf{W}}^{-}(z_0, z_{n+1})\,\mathbf{R}^{\cup}(z_{n+1})\,\mathbf{W}(z_{n+1}, z_n)$;
  **for** $\mathbf{c} \in \{\mathbf{c}_\alpha, \mathbf{c}_\beta, \mathbf{c}_\rho\}$ **do**
    Calculate $\Delta\mathbf{c}^{R^{\cap}}(z_n)$ and $\Delta\mathbf{c}^{T^{+}}(z_n)$;
    $\Delta\mathbf{c}(z_n) = \Delta\mathbf{c}(z_n) + \Delta\mathbf{c}^{R^{\cap}}(z_n) + \Delta\mathbf{c}^{T^{+}}(z_n)$;
  **end**
**end**

## 3 RESULTS

In this section, we show the results of applying algorithm 2 on two synthetic models. First, we examine a flat, layered model, which will serve as a proof-of-concept and allows us to explore the properties of the inversion results generated by the method. Secondly, we examine a model featuring a lens-shaped inclusion with a large contrast with respect to the surroundings. This model represents a simplified version of a salt body in the subsurface, which is a difficult situation to image properly if converted waves are not taken into account.

### 3.1 Flat layered model

We begin our analysis with a simple, flat, layered model, based on the model used by Wu *et al.* (2022). This model will serve as a toy model, which is used to benchmark the proposed method. It has been constructed such that the $S$-wave velocity $\beta$ in the middle layer is close to the $P$-wave velocity $\alpha$ in the surrounding layers, as shown in Figs 2(a)–2(c), which represents the case of a salt body within the subsurface.

Synthetic data was generated for the aforementioned model using 61 $P$-wave sources evenly spaced along the surface. The source wavelet used was a Ricker wavelet with a peak frequency of 17 Hz. Both $P$- and $S$-wave data was recorded with 301 receivers with a receiver spacing of 10 m. To avoid an inverse crime scenario (where the same modelling engine is used for both forward and inverse modelling), elastic Kennett modelling (Kennett 1984) was used to generate the synthetic data. This data was then filtered in the spatial Fourier domain to remove post-critical effects, as we know that the extended Shuey approximations used for the reflection and transmission operators only hold up to the critical angle. Migration was then performed on the synthetic data using algorithm 2, with a smoothed version of the true velocity models used for the propagation velocities. Forward and inverse modelling was performed on a grid of 301 by 151 points, with a lateral spacing of 10 m and a vertical spacing of 5 m. For the extended Shuey approximations, Taylor expansions up to $K = 6$ and $\Lambda = 2$ were used. The results of this process are shown in Figs 2 and 3.

We now analyse these results, starting with Fig. 2, which show the true $P$-wave velocity contrast $c_\alpha$, $S$-wave velocity contrast $c_\beta$ and density contrast $c_\rho$, along with the inverted contrasts after 10 iterations. We begin our analysis with the reconstructed $S$-wave velocity contrast $c_\beta$, shown in Fig. 2(e), which we see matches the ground truth quite closely, with both reflectors clearly identifiable. The reconstructed density contrast $c_\rho$, shown in Fig. 2(f), also clearly shows both reflectors, but contains some smearing above the top reflector. Finally, the reconstructed $P$-wave velocity contrast $c_\alpha$, shown in Fig. 2(d), struggles in this case, with the two reflectors not being clearly visible.

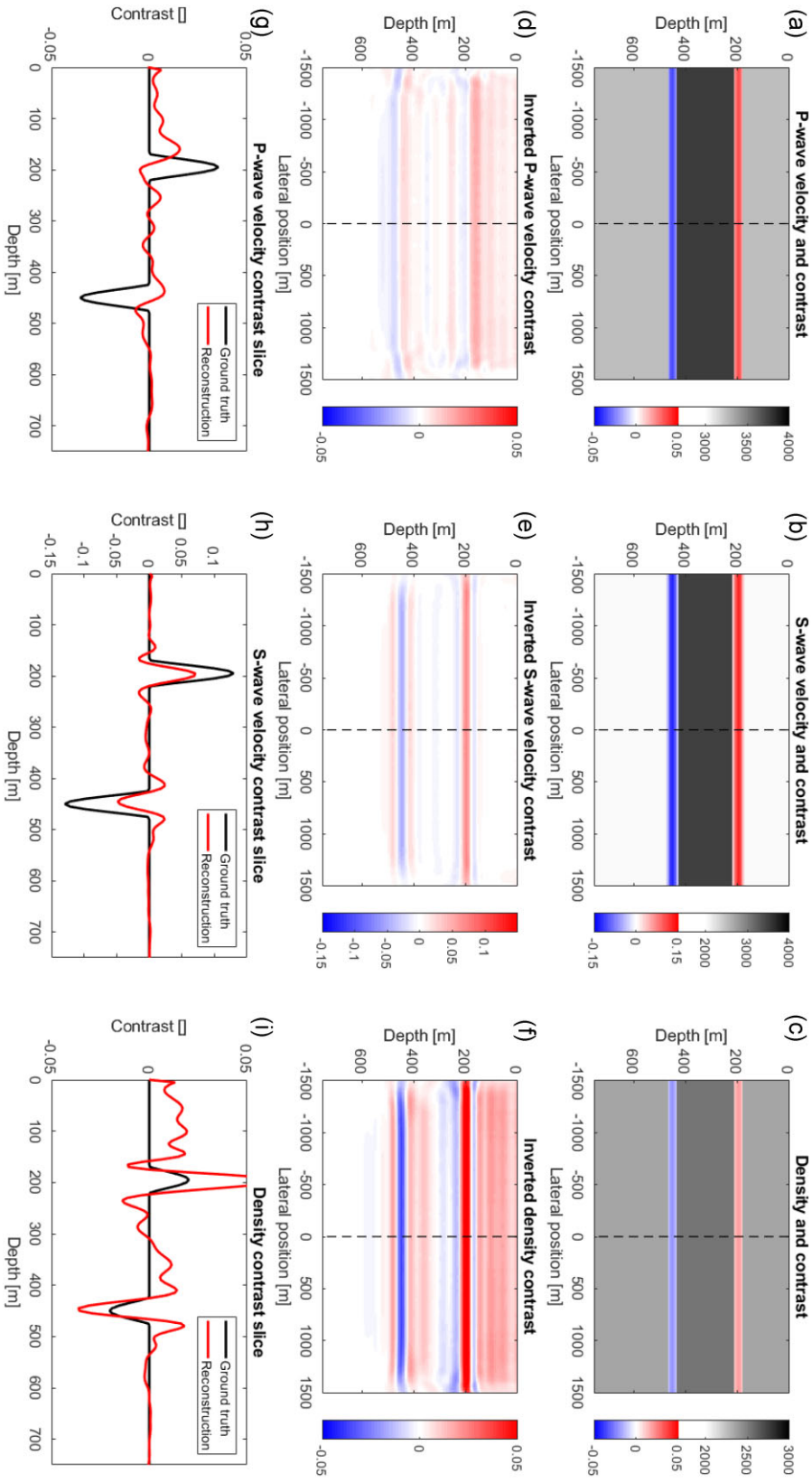


**Figure 2.** Results of elastic FWM for the flat, layered model. The ground-truth $P$-wave velocity, $S$-wave velocity and density, along with their contrasts, are shown in panels (a), (b) and (c), respectively. The reconstructed $P$-wave velocity, $S$-wave velocity and density contrasts after 10 iterations are shown in figures (d), (e) and (f), respectively. Finally, the ground-truth $P$-wave velocity, $S$-wave velocity and density contrasts at $x = 0$ (black lines), as well as the reconstructed contrasts (red lines), are shown in figures (g), (h) and (i), respectively.

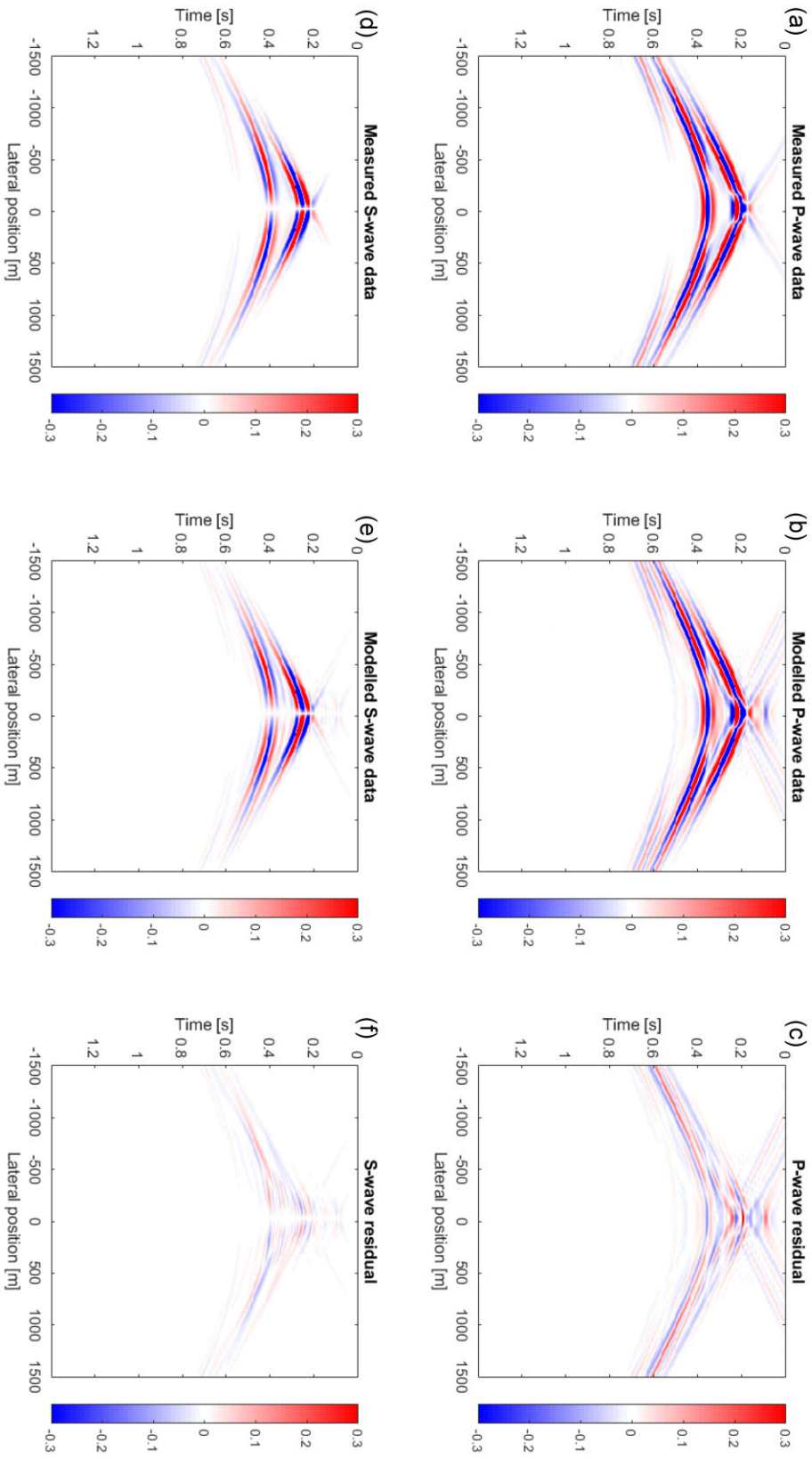


**Figure 3.** Shot records for the flat, layered model. The synthetic *P*- and *S*-wave data, generated by elastic Kennett modelling, are shown in panels (a) and (d), respectively. The forward modelled *P*- and *S*-wave data after 10 iterations is shown in panels (b) and (e), respectively. Finally, the difference between the synthetic *P*- and *S*-wave data and the forward modelled data is shown in panels (c) and (f), respectively. All wavefields have been normalized with respect to the maximum amplitude of the synthetic *P*- and *S*-wave data, respectively.

For a more detailed analysis, we examine slices taken through the centre of Figs 2(d)–2(f), which are shown in Figs 2(g)–2(i). From these figures, we see a similar pattern. Once again, we see that the results for $c_\beta$ match the (band-limited) ground truth quite well. The result for $c_\rho$ introduces additional smearing, and also clearly overestimates the strength of the contrast. Finally, the result for $c_\alpha$ does not accurately reproduce the two reflectors.

To explore the reasons behind the lack of accuracy in the results for $c_\rho$ and $c_\alpha$, we examine the cross-talk between the different parameters. We begin by investigating $\left(\tilde{R}^{\cup}_{PP}\right)^0_1$, the lowest order component of the $PP$-reflectivity, which is given by

$$\left(\tilde{R}^{\cup}_{PP}\right)^0_1 = \frac{1}{2}\left(c_\alpha + c_\rho\right). \tag{73}$$

From this expression, we see that there is strong cross-talk between the $c_\alpha$ and $c_\rho$ terms for near-zero angles of incidence. In the same vein, we examine $\left(\tilde{R}^{\cup}_{SP}\right)^1_1$, the lowest order component of the $SP$ reflectivity, which is given by

$$\left(\tilde{R}^{\cup}_{SP}\right)^1_1 = -\left(\hat{V}\left(c_\rho + 2c_\beta\right) + \frac{1}{2}c_\rho\right), \tag{74}$$

where $\hat{V} = \beta/\alpha$. From this expression, we see that there is also cross-talk between the $c_\beta$ and $c_\rho$ terms. This cross-talk between separate contrasts may explain why the density contrast $c_\rho$ is overestimated, while the $P$-wave velocity contrast $c_\alpha$ is simultaneously underestimated. A possible approach to reduce this cross-talk is to apply some form of pre-conditioning, such as pre-conditioning the gradient with the inverse of the Hessian (Abolhassani & Verschuur 2024).

To complete our analysis of the flat, layered example we examine a shot record, seen in Fig. 3. Note the strong converted wave response in the $P$-wave data shown in Fig. 3(a), visible below the primary $PP$-reflection from the 'base-salt'. From Fig. 3(d) we see that this converted wave response is due to $PPSP$ and $PSPP$ wave paths in the medium, as the $PSSS$ response is very small. Examining Figs 3(b) and 3(e), we see that the method has generally been able to capture much of the converted wave response. This is confirmed by the residuals, shown in Figs 3(c) and 3(f).

### 3.2 Lens-shaped inclusion model

In this section we will examine a so-called lens-shaped inclusion model, with a lens with a large contrast in the centre of the model and a number of flat layers beneath it. In the same way as for the flat, layered model, the parameters of the lens have been chosen such that the $S$-wave velocity inside the lens matches the $P$-wave velocity outside the lens, representing a high-contrast salt body.

To generate data for the aforementioned model, a finite-difference time-domain modelling scheme was used (4th order in space, 2nd order in time) (Thorbecke & Draganov 2011). In total, 61 sources were used with a source spacing of 50 m, together with 301 receivers with a receiver spacing of 10 m. The source wavelet employed was a Ricker wavelet with a peak frequency of 17 Hz. Once again, post-critical effects were filtered from the data in the spatial Fourier domain. Next, elastic FWM was applied on the synthetic data, using a grid of 301 by 381 points, with a grid spacing of 10 m in the lateral direction and 5 m in the vertical direction. Smoothed versions of the true velocity models were used for the propagation velocities. For the extended Shuey approximations, Taylor expansions up to $K = 8$ and $\Lambda = 2$ were used. The ground-truth contrasts, as well as the inversion results after five iterations, are shown in Fig. 4.

Examining the inverted contrasts, we see many of the same effects as those we observed for the flat, layered model in the previous section. Once again starting with the $S$-wave velocity contrast $c_\beta$, shown in Fig. 4(e), we see that the lens has been recovered well in this case. However, the deeper reflectors are not well resolved. This is probably due to the fact that these deeper reflectors are only illuminated by small angles of incidence, which are not sensitive to the $S$-wave velocity contrast $c_\beta$, making it difficult to reconstruct properly.

Continuing our analysis, we examine the density contrast $c_\rho$, shown in Fig. 4(f). Once again, we note that the density contrast has been overestimated in this case, similar to the results of the flat model, shown in 2(f). We also note additional smearing above the top reflector in this case. The $P$-wave velocity contrast $c_\alpha$, shown in Fig. 4(d), also shows similar results. Most notably, the top part of the lens is not reconstructed well in this case, while the deeper layers are recovered accurately. These observations are further confirmed by examining slices through the centre of Figs 4(d)–4(f), shown in Figs 4(g)–4(i). Once again, it appears that cross-talk between the different contrasts has made it difficult to accurately recover the separate contrasts in this case.

Finally, we examine a shot record for the lens inclusion model, shown in Fig. 5. Comparing the forward modelled wavefields, shown in Figs 5(b) and 5(e), to the finite-difference data shown in Figs 5(a) and 5(d), we see that the method explains the data reasonably well. However, the residuals, shown in Figs 5(c) and 5(f), are clearly larger than those achieved for the flat model, shown in Figs 3(c) and 3(f). This increased residual is probably caused by inaccuracies in the modelling of the dipping reflectors, which are difficult to model accurately when using one-way operators.

## 4 DISCUSSION

In this section we will discuss some additional aspects regarding the elastic FWM method presented in this paper. First, we compare the results shown in Section 3 to the results of the conventional, acoustic FWM method for the same models. Next, we examine the case where no $S$-wave data is available, such as in a marine setting. Finally, we discuss a number of potential extensions of the elastic FWM method.

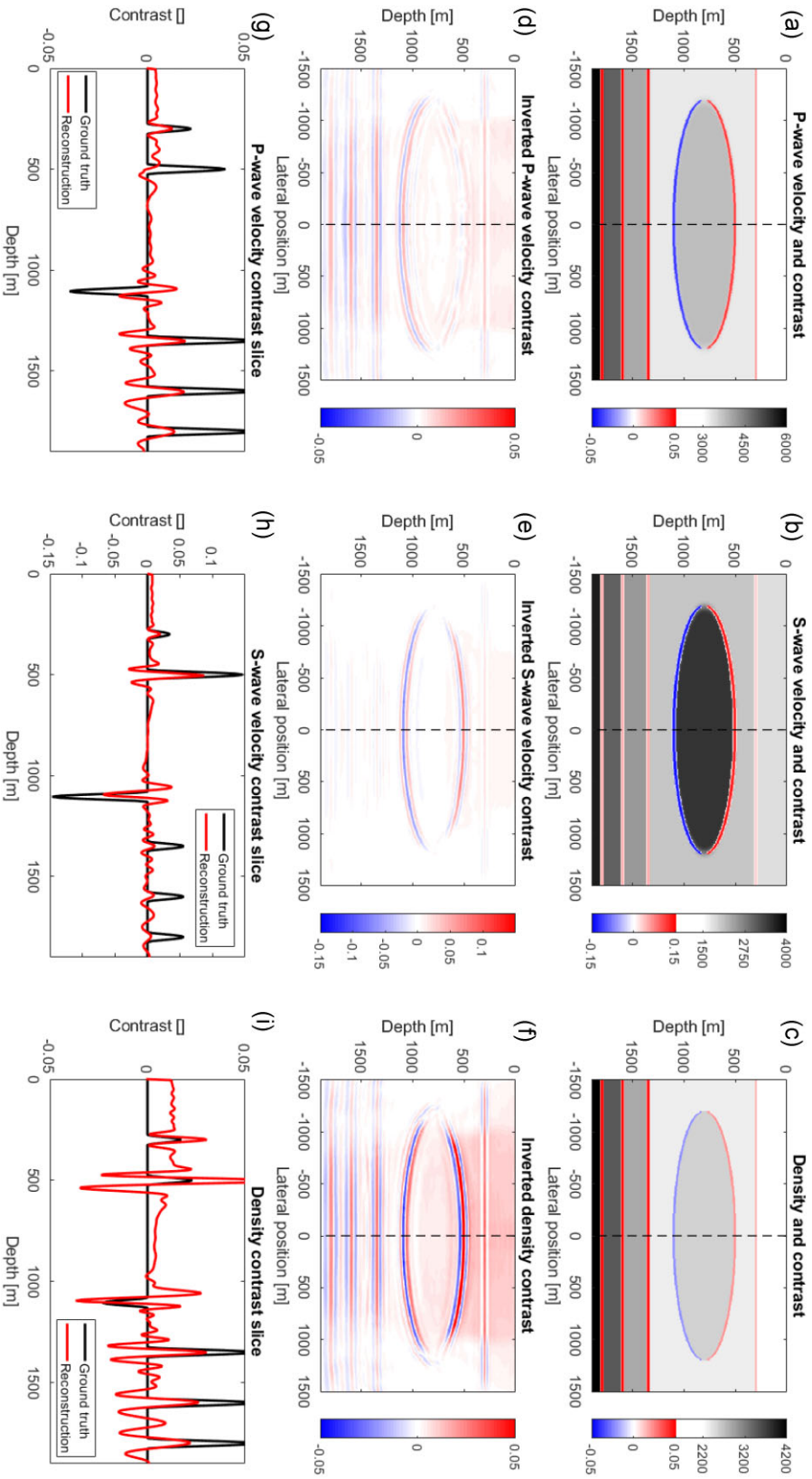


**Figure 4.** Results of elastic FWM for the lens-shaped inclusion model. The ground-truth $P$-wave velocity, $S$-wave velocity and density, along with their contrasts, are shown in panels (a), (b) and (c), respectively. The reconstructed $P$-wave velocity, $S$-wave velocity and density contrasts after five iterations are shown in panels (d), (e) and (f), respectively. Finally, the ground-truth $P$-wave velocity, $S$-wave velocity and density contrasts at $x = 0$ (black lines), as well as the reconstructed contrasts (red lines), are shown in panels (g), (h) and (i), respectively.

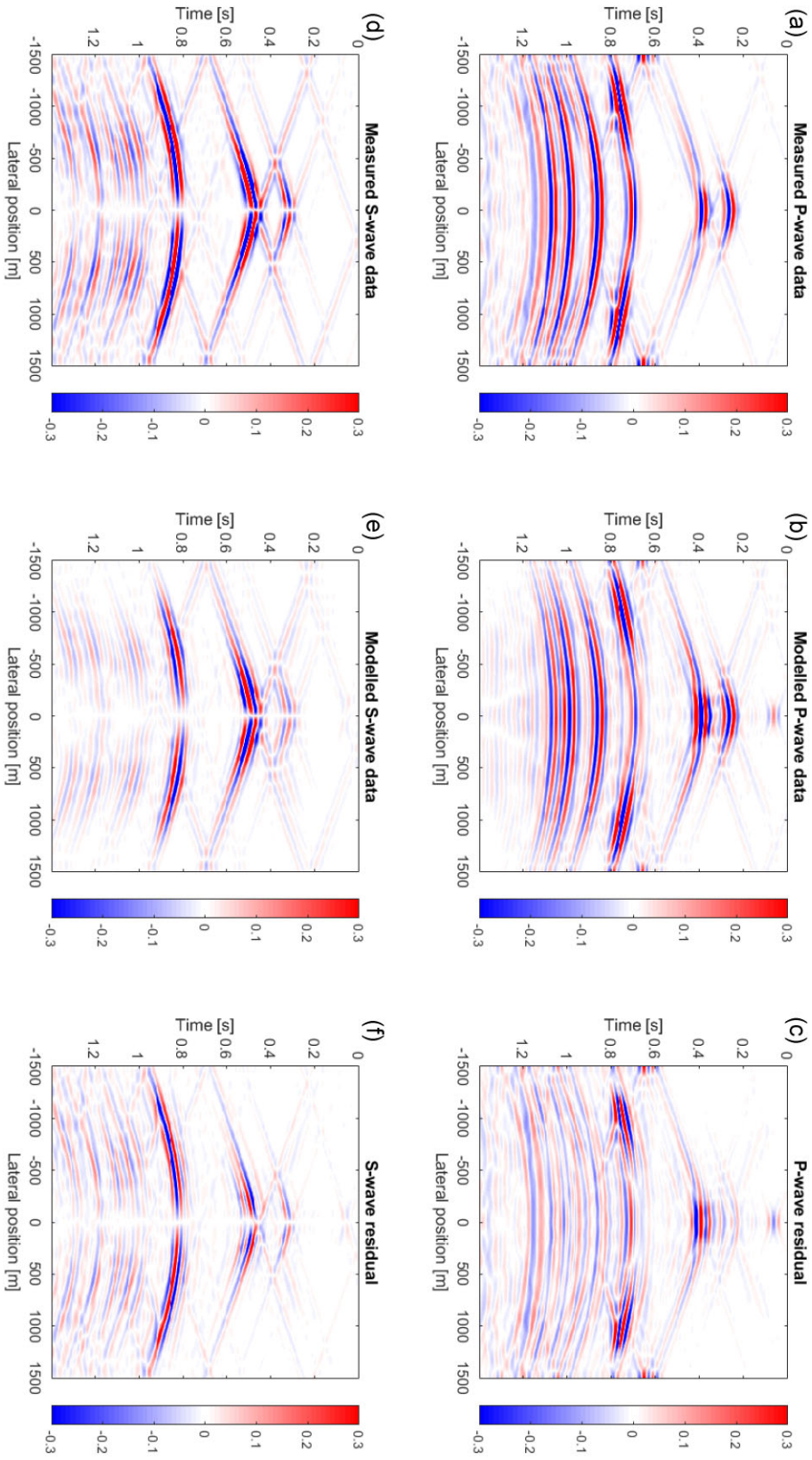


**Figure 5.** Shot records for the lens-shaped inclusion model. The synthetic *P*- and *S*-wave data, generated by elastic, time-domain finite-difference modelling, are shown in panels (a) and (d), respectively. The forward modelled *P*- and *S*-wave data after five iterations are shown in panels (b) and (e), respectively. Finally, the difference between the synthetic *P*- and *S*-wave data and the forward modelled data are shown in panels (c) and (f), respectively. All wavefields have been normalized with respect to the maximum amplitude of the synthetic *P*- and *S*-wave data, respectively.

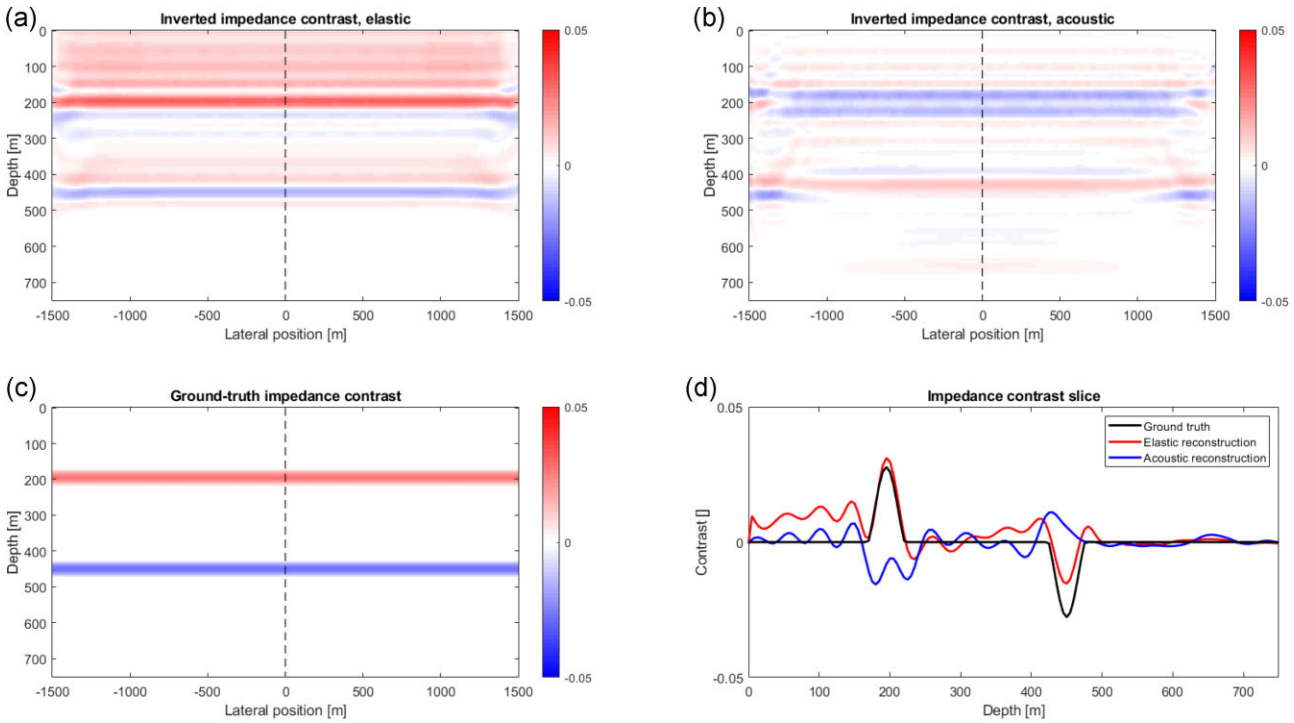


**Figure 6.** Comparison of elastic FWM and acoustic FWM for the flat, layered model. The reconstructed impedance contrast generated by elastic FWM and acoustic FWM after 10 iterations are shown in panels (a) and (b), respectively. The ground-truth impedance contrast is shown in panel (c). Finally, a slice through panels (a)–(c) is shown in panel (d), showing the ground-truth impedance contrast (black line), the elastic FWM result (red line) and the acoustic FWM result (blue line).

### 4.1 Comparison to acoustic FWM

We begin by comparing the results for the elastic FWM algorithm with the conventional, angle-independent, acoustic FWM algorithm. In the acoustic FWM algorithm, the quantity of interest for inversion is the impedance contrast $c_Z$, which is defined as

$$c_Z = \frac{1}{2}\left(c_\alpha + c_\rho\right). \tag{75}$$

Therefore, in order to compare the reconstructions of the acoustic and elastic FWM methods fairly, we will compare the acoustic FWM image to the average of the reconstructed $P$-wave velocity and density contrasts. Note that this comparison does not take into account the fact that the elastic FWM algorithm provides additional information by separating the contrasts, thus giving more insight into the underlying medium properties.

We begin by comparing the elastic and acoustic FWM results for the flat model described in Section 3.1. The reconstructed impedance contrasts are shown in Fig. 6. Comparing Figs 6(a) and 6(b), we immediately note that the acoustic FWM algorithm is not able to reconstruct the reflectors properly in this case. Most notably, the acoustic FWM image has flipped the sign of the reflectors. This is easily explained by examining the shot records, shown in Fig. 7. Examining the true $P$-wave data, shown in Fig. 7(a), we note that the reflectivity goes from positive to negative at offsets away from zero incidence. As the acoustic FWM algorithm assumes the reflectivity to be angle-independent, it is unable to account for this effect, leading to it estimating the reflectivity with the wrong sign. Note that this is a rather extreme case, as the change in reflectivity at different angles is usually less strong.

Examining a slice through the middle of Figs 6(a) and 6(b), shown in Fig. 6(d), we see this effect more clearly. From this figure, we also see that, while the elastic FWM result introduces some smearing for depths above the first reflector, the overall result for elastic FWM is more consistent. Specifically, the two reflectors are clearly recovered, with no spurious reflectors introduced below the bottom reflector. The acoustic FWM image, on the other hand, does not recover the two reflectors well, and is less consistent for areas below the top reflector. Note that the smearing present in the elastic FWM result can be easily removed by filtering out the lowest spatial frequencies present in the image.

Next, we compare the modelled $P$-wave data for elastic FWM, shown in Fig. 7(b), and acoustic FWM, shown in Fig. 7(e). Comparing these figures, we see that the modelled wavefield for elastic FWM is more consistent than that of acoustic FWM. Most notably, the wavefield recovered by elastic FWM captures wave-conversion effects accurately, while the acoustic method is unable to take these effects into account. This leads to a significantly larger data residual when using acoustic FWM, as is shown in Fig. 7(f).

Finally, we compare the elastic and acoustic FWM results for the lens-shaped inclusion model, described in Section 3.2. The results for this comparison are shown in Fig. 8. Comparing Figs 8(a) and 8(b), we note that the acoustic FWM algorithm is unable to reconstruct the top of the lens-shaped inclusion properly, which the elastic FWM algorithm is able to do. This is confirmed by Fig. 8(d), which shows that

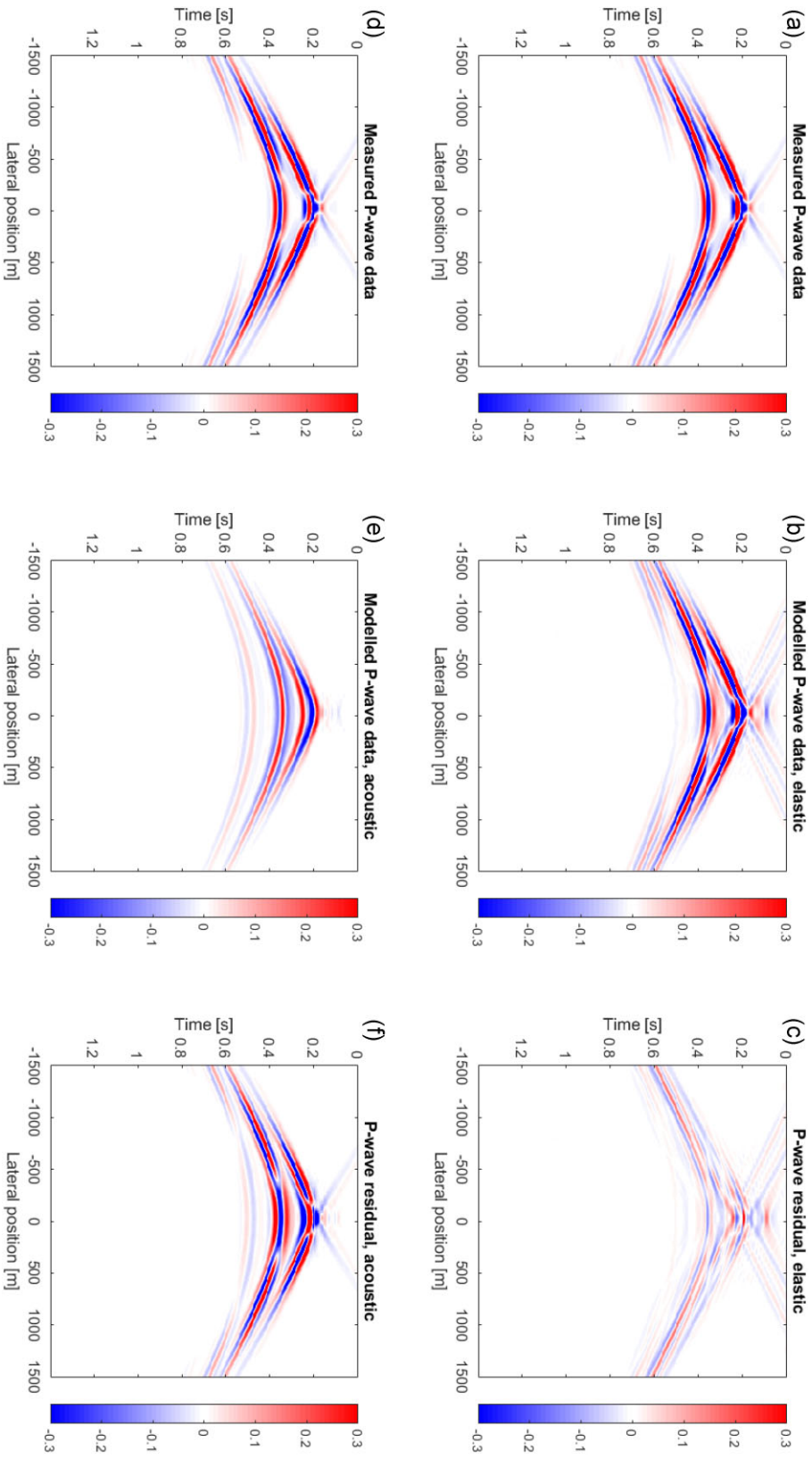


**Figure 7.** Shot records for the flat, layered model. The synthetic $P$-wave data, generated by elastic Kennett modelling, is shown in panels (a) and (d). The forward modelled $P$-wave data for elastic FWM and acoustic FWM after 10 iterations are shown in panels (b) and (e), respectively. Finally, the difference between the synthetic $P$-wave data and the forward modelled data for elastic FWM and acoustic FWM are shown in panels (c) and (f), respectively. All wavefields have been normalized with respect to the maximum amplitude of the synthetic $P$-wave data.

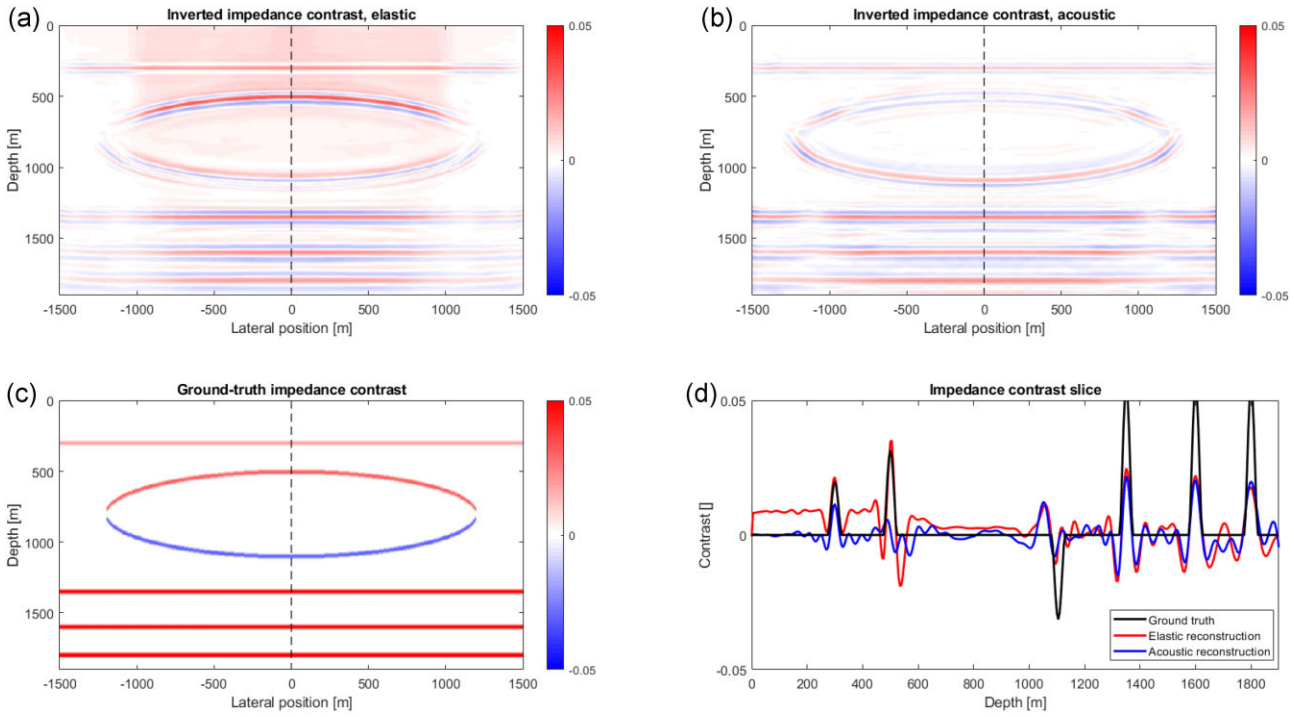


**Figure 8.** Comparison of elastic FWM and acoustic FWM for the lens-shaped inclusion model. The reconstructed impedance contrast generated by elastic FWM and acoustic FWM after five iterations are shown in panels (a) and (b), respectively. The ground-truth impedance contrast is shown in panel (c). Finally, a slice through panels (a)–(c) is shown in panel (d), showing the ground-truth impedance contrast (black line), the elastic FWM result (red line) and the acoustic FWM result (blue line).

the top of the lens is recovered well in elastic FWM while being absent in the acoustic result. While the elastic FWM method does introduce additional smearing above the top reflector, this can once again be removed by filtering the final result.

### 4.2 Missing *S*-wave data

In this section, we examine the results of the elastic FWM algorithm in cases where only $P$-wave data is available. This situation corresponds to a marine acquisition scenario, for example, where no $S$-waves can be recorded.

We begin by examining the results for the flat model of Section 3.1, which are shown in Fig. 9. Examining the reconstructed contrasts, shown in Figs 9(d)–9(f), we note a number of differences compared to the reconstructed contrasts when $S$-wave data is available, shown in Figs 2(d)–2(f). Most notably, we see that the $S$-wave velocity contrast $c_\beta$ is significantly less well recovered when no $S$-wave data is available. This is to be expected, as the $SP$-reflection coefficient depends much more strongly on $c_\beta$ than the $PP$-reflection coefficient. In cases where there is no $S$-wave data available, therefore, the objective function $J$ does not depend as strongly on $c_\beta$. This makes it more difficult to recover accurately. The other contrasts, however, are comparable with the results when $S$-wave data is available.

Next, we examine the results for the lens-shaped inclusion model of Section 3.2, which are shown in Fig. 10. Once again, we compare Figs 10(d)–10(f) with Figs 4(d)–4(f). In this case, we once again note that the $S$-wave velocity contrast is significantly less well recovered when no $S$-wave data is available. However, once again we note that the results for the density contrast and the $P$-wave velocity contrast are comparable to the case where $S$-wave data is available. This indicates that the elastic FWM algorithm can be used successfully in marine cases, where no direct $S$-wave data is available.

### 4.3 Possible extensions

Finally, in this section, we examine a number of possible extensions to the elastic FWM algorithm presented in this paper. We begin by examining the local dip $\theta_0$, which we have assumed to be known in Section 2.3. In cases where the local dip is not known *a priori*, one can begin by using a conventional, acoustic imaging technique, such as angle-independent acoustic FWM, to generate an initial model of the reflectivity. By applying a local dip estimation scheme on this preliminary image, one can find an estimate of the local dip, which can be used as an input for the method presented here. In the case of the lens model presented in Section 3.2, the local dip was estimated by applying a dip estimation scheme on the ground-truth reflectors, capping the maximal dip angle at 30 degrees.

Alternatively, one can estimate the local dip directly from the reflection operators, by extending the inversion process described in Section 2.4 to include the local dip angle. To do this, one requires the derivative of the objective function $J$ with respect to $\theta_0(x_i, z_n)$.

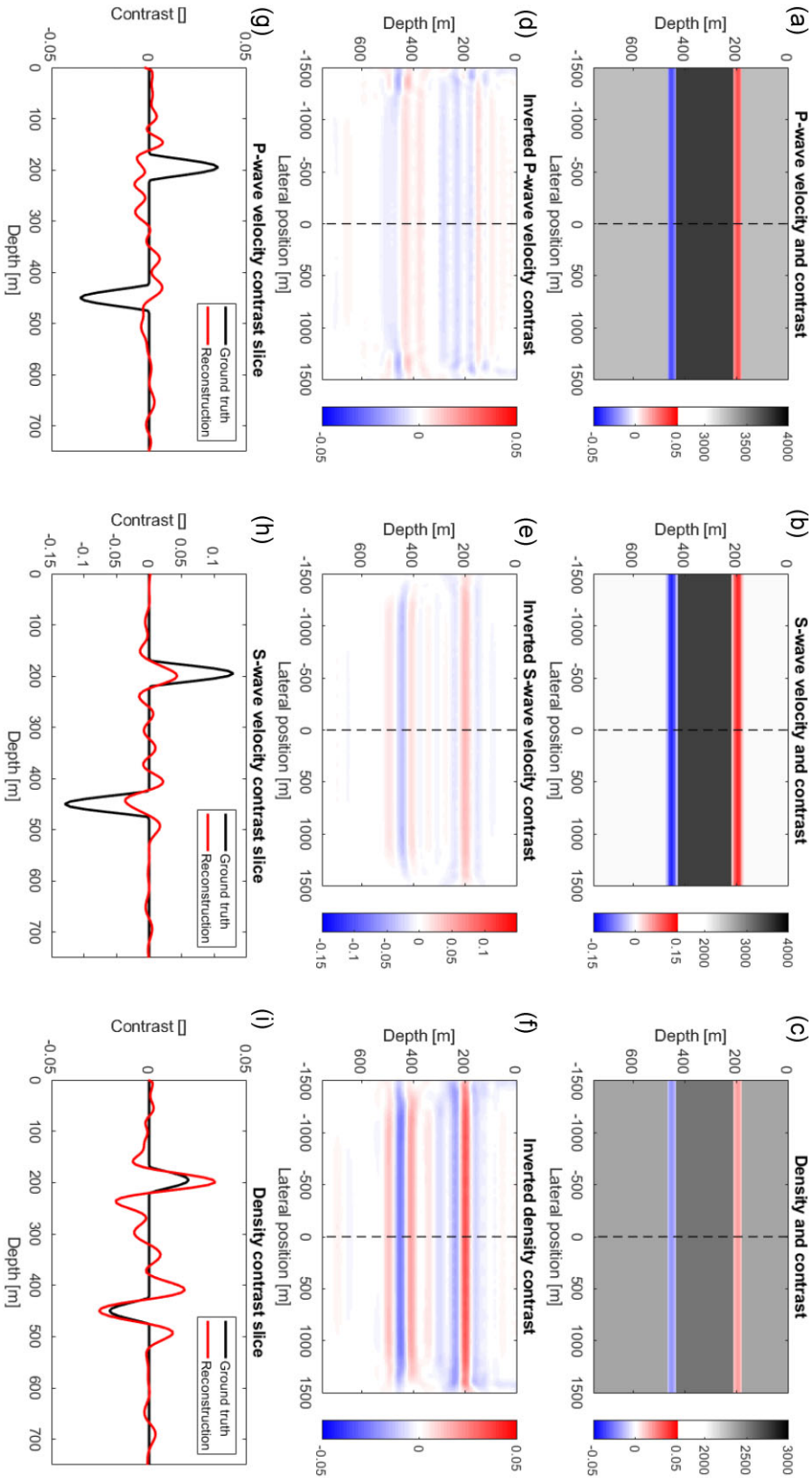


**Figure 9.** Results of elastic FWM for the flat, layered model when no $S$-wave data is available. The ground-truth $P$-wave velocity, $S$-wave velocity and density, along with their contrasts, are shown in figures (a), (b) and (c), respectively. The reconstructed $P$-wave velocity, $S$-wave velocity and density contrasts after 10 iterations are shown in figures (d), (e) and (f), respectively. Finally, the ground-truth $P$-wave velocity, $S$-wave velocity and density contrasts at $x = 0$ (black lines), as well as the reconstructed contrasts (red lines), are shown in figures (g), (h) and (i), respectively.

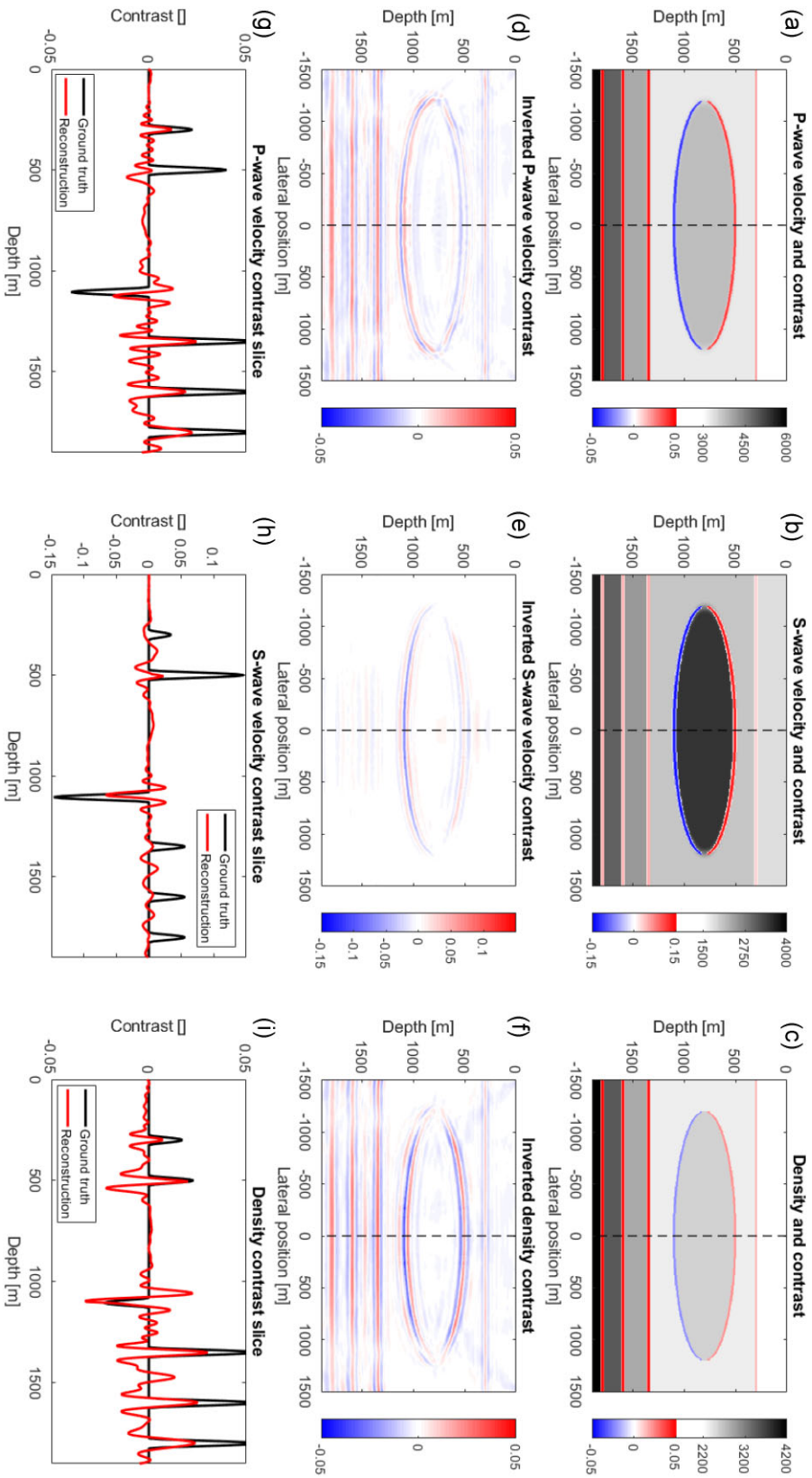


**Figure 10.** Results of elastic FWM for the lens-shaped inclusion model when no *S*-wave data is available. The ground-truth *P*-wave velocity, *S*-wave velocity and density, along with their contrasts, are shown in panels (a), (b) and (c), respectively. The reconstructed *P*-wave velocity, *S*-wave velocity and density contrasts after 10 iterations are shown in panels (d), (e) and (f), respectively. Finally, the ground-truth *P*-wave velocity, *S*-wave velocity and density contrasts at $x = 0$ (black lines), as well as the reconstructed contrasts (red lines), are shown in panels (g), (h) and (i), respectively.

Summarizing the analysis of Section 2.4, we find that this derivative is proportional to the derivative of the reflection and transmission operators. Examining the $PP$-reflection operator, we find

$$\frac{\partial \mathbf{R}^{\cup}_{PP}(z_n)\big|_{ij}}{\partial \theta_0(x_i, z_n)} \approx \sum_{\kappa=0}^{K}\sum_{\kappa'=0}^{K}\sum_{\lambda=0}^{\Lambda} \left(\tilde{\mathbf{R}}^{\cup}_{PP}\right)^{\kappa'}_{\lambda}(z_n)\Big|_{ij} \frac{\partial \mathbf{S}^{\kappa'}_{\kappa}(\theta_0)\big|_{ii}}{\partial \theta_0(x_i, z_n)} \delta_{ij}\, \mathbf{S}^{\kappa}_{\theta}(z_n)\big|_{ij}, \tag{76}$$

which can be straightforwardly evaluated using mathematical software. Using these derivatives, the local dip can be updated at each iteration in a similar way to the contrasts. In this manner, the estimation of the local dip can be integrated into the elastic FWM framework with little additional effort.

Secondly, while the results presented in this paper have been achieved in the 2-D case, the method can also be extended to 3-D applications, in a similar way as the conventional, acoustic FWM method (Davydenko & Verschuur 2017). In the 3-D case, the 1-D convolutions of the 2-D method need to be replaced with 2-D convolutions to account for the propagation and scattering in three dimensions. An additional challenge for elastic FWM is that it is necessary to take $S_H$ waves into account as well as the $S_V$ waves that we have discussed in this paper. In principle, these waves can be taken into account using the same framework as presented here. However this will introduce additional complexity into the presented algorithm, and is outside the scope of this paper.

Thirdly, in situations where significant wave conversions are only expected within a specific region of interest, it is possible to adapt the method to focus specifically on this region. Due to the use of explicit reflection and transmission operators, it is possible to apply angle-independent, acoustic imaging in the over- and underburden of the region of interest (by setting $K = 0$ and $\Lambda = 1$, for example), while still taking all wave conversions within the region of interest into account. This further reduces the computational cost of the method, while still taking the most critical converted wave events into account. Note that this separation is difficult to apply in methods such as elastic RTM and elastic FWI, due to the implicit nature of the modelling engines commonly used in these approaches.

Finally, the elastic FWM algorithm presented here can be incorporated into a joint reflectivity and velocity estimation algorithm, such as joint migration inversion (JMI) (Berkhout 2014c; Staal 2015) or one-way reflection waveform inversion (ORWI) (Abolhassani & Verschuur 2023). In conventional, acoustic JMI it is difficult to incorporate angle-dependent reflectivity, as estimating both the angle-dependent reflectivity and the velocity model simultaneously leads to overparametrization (Qu 2020). However, by using the extended Shuey's approximations of Section 2.3, the number of parameters required to estimate the angle-dependent reflectivity is significantly reduced. This could potentially allow one to estimate both angle-dependent reflectivity along with velocity simultaneously. By further extending the acoustic JMI algorithm to also include $S$-wave velocity estimation, an elastic JMI algorithm, which takes converted waves into account, could finally be developed.

## 5 CONCLUSIONS

In conventional, acoustic full wavefield migration, we neglect wave conversions from $P$ to $S$ waves, as well as the propagation of $S$ waves throughout the medium. In this paper, we have presented an extension to the acoustic FWM algorithm which takes these effects into account using an extended version of Shuey's approximation.

Our main conclusion, based on the results we have presented, is that elastic FWM outperforms acoustic FWM in cases with large contrasts, where strong AVO and wave-conversion effects are present. While the reconstructed contrasts are not perfect, they are an improvement compared to the acoustic FWM results for the same areas. Therefore, we conclude that elastic FWM serves as an effective extension of acoustic FWM for these situations and can serve to improve the resulting images in areas with strong converted waves.

Furthermore, we show that the method can still produce accurate results in cases where $S$-wave data is not available, such as in marine settings. This makes the method more widely applicable. We also present several possible areas where the method can be extended, which can serve to further increase the potential of the method.

## ACKNOWLEDGMENTS

The authors thank the sponsoring companies from the Delphi Consortium at Delft University of Technology for their support to this research.

## DATA AVAILABILITY

The synthetic data used in this paper is available upon request. Due to agreements made with the sponsoring companies of the Delphi Consortium, we are unable to share the code used to generate the results of this paper.

## REFERENCES

Abolhassani, S. & Verschuur, D.J., 2024. Efficient preconditioned least-squares wave-equation migration, *Geophysics,* **89,** 275–288.

Abolhassani, S. & Verschuur, E., 2023. High-resolution one-way reflection waveform inversion, in *EAGE Annual Conference and Exhibition 2023,* EAGE, Vienna, Austria.

Aki, K. & Richards, P.G., 2002. *Quantitative Seismology,* 2nd edn, University Science Books.

Alai, R. *et al.*, 2022. Improved subsalt imaging in Brazil Campos basin—Cascaded application of hybrid interbed demultiple, *P*- and *S*-salt velocity joint migration, and subsalt converted wave suppression, *SEG Technical Program Expanded Abstracts,* 2680–2684.

Alai, R. *et al.*, 2021. Enhancing subsalt imaging through advanced identification and suppression of interbed multiples and mode-converted reflections—Gulf of Mexico and Brazil case studies, *Leading Edge,* **40,** 905–913.

Berkhout, A. J., 2014a. Review Paper: An outlook on the future of seismic imaging, Part I: forward and reverse modelling, *Geophys. Prospect.,* **62,** 911–930.

Berkhout, A.J., 2014b. Review paper: an outlook on the future of seismic imaging, Part II: full-wavefield migration, *Geophys. Prospect.,* **62,** 931–949.

Berkhout, A.J., 2014c. Review Paper: An outlook on the future of seismic imaging, Part III: joint migration inversion, *Geophys. Prospect.,* **62,** 950–971.

Berkhout, A.J., 2012. *Seismic migration: Imaging of Acoustic Energy by Wave Field Extrapolation: Imaging of Acoustic Energy by Wave Field Extrapolation,* Elsevier.

Chang, W.-F. & McMechan, G.A., 1987. Elastic reverse-time migration, *Geophysics,* **52,** 1365–1375.

Davydenko, M. & Verschuur, D.J., 2017. Full-wavefield migration: using surface and internal multiples in imaging, *Geophys. Prospect.,* **65,** 7–21.

Ensley, R.A., 1984. Comparison of *P*- and *S*-wave seismic data: A new method for detecting gas reservoirs, *Geophysics,* **49,** 1420–1431.

Fomel, S., 2002. Applications of plane-wave destruction filters, *Geophysics,* **67,** 1946–1960.

Gisolf, D. & Verschuur, E., 2010. *The Principles of Quantitative Acoustical Imaging,* EAGE Publications bv.

Hammad, H.I. & Verschuur, D.J., 2018. Generalized Full Wavefield Modeling: Beyond Neumann, *80th EAGE Annual Conference & Exhibition* **2018,** 1–5.

Hoogerbrugge, L., van Dongen, K.W.A. & Verschuur, D.J., 2025. Extending Shuey's approximation using Taylor expansions for forward and inverse modelling, *Geophysical Journal International* **241,** 876–890.

Jones I, F. & Davison, I., 2014. Seismic imaging in and around salt bodies, *Interpretation,* **2,** 1N–T284.

Kennett, B.L.N., 1984. An operator approach to forward modeling, data processing and migration, *Geophys. Prospect.,* **32,** 1074–1090.

Li, A. & Liu, X., 2021. An optimised one-way wave migration method for complex media with arbitrarily varying velocity based on eigen-decomposition, *J. Geophys. Eng.,* **18,** 776–787.

Mulder, W.A. & Plessix, R.-E., 2004. A comparison between one-way and two-way wave-equation migration, *Geophysics,* **69,** 1491–1504.

Oppenheim, A.V., Willsky, A.S. & Nawab, S.H., 1996. *Signals and Systems,* 2nd edn, Pearson.

Prieux, V., Brossier, R., Operto, S. & Virieux, J., 2013. Multiparameter full waveform inversion of multicomponent ocean-bottom-cable data from the Valhall field. Part 2: imaging compressive-wave and shear-wave velocities, *J. geophys. Int.,* **194,** 1665–1681.

Qu, S., 2020. *Simultaneous joint migration inversion as a high-resolution time-lapse imaging method for reservoir monitoring,* PhD thesis, Delft University of Technology.

Ren, Z., Liu, Y. & Sen, M.K., 2017. Least-squares reverse time migration in elastic media, *J. geophys. Int.,* **208,** 1103–1125.

Shuey, R.T., 1985. A simplification of the Zoeppritz equations, *Geophysics,* **4,** 530–743.

Staal, X., 2015. *Combined imaging and velocity estimation by Joint Migration Inversion,* PhD thesis, Delft University of Technology.

Sun, Y., Kim, Y.S., Qu, S., Verschuur, E., Almomin, A. & van Borselen, R., 2018. Angle-dependent full-wavefield migration based upon full-waveform inversion and joint-migration inversion, *SEG Technical Program Expanded Abstracts* 4357–4361.

Thorbecke, J.W. & Draganov, D., 2011. Finite-difference modeling experiments for seismic interferometry, *Geophysics,* **76,** doi: 10.1190/geo2010-0039.1.

Virieux, J. & Operto, S., 2009. An overview of full-waveform inversion in exploration geophysics, *Geophysics,* **74,** 1–26.

Wapenaar, C.P.A. & Grimbergen, J.L.T., 1996. Reciprocity theorems for one-way wave fields, *J. geophys. Int.,* **127,** 169–177.

Wu, Z., Wei, Z., Zhang, Z., Mei, J., Huang, R. & Wang, P., 2022. Elastic FWI for large impedance contrasts, *SEG Technical Program Expanded Abstracts* 3686–3690.

## APPENDIX A: EXPLICIT EXPRESSIONS FOR THE UPDATE DIRECTION

In Section 2.4 we have discussed the update direction for the contrasts $c_\chi$, viz.

$$\Delta \mathbf{c}_\chi(z_n) = \sum_\omega \sum_s \left[ \Delta \mathbf{c}_\chi^{R^\cup}(z_n) + \Delta \mathbf{c}_\chi^{R^\cap}(z_n) + \Delta \mathbf{c}_\chi^{T^+}(z_n) + \Delta \mathbf{c}_\chi^{T^-}(z_n) \right], \tag{A1}$$

with $\chi \in \{\alpha, \beta, \rho\}$. In this section we explicitly write the individual components of the update for ease of reference.

We begin by examining the terms $\Delta \mathbf{c}_\chi^{R^\cup}$, $\Delta \mathbf{c}_\chi^{R^\cap}$, $\Delta \mathbf{c}_\chi^{T^+}$ and $\Delta \mathbf{c}_\chi^{T^-}$, viz.

$$\begin{aligned}\Delta \mathbf{c}_\chi^{R^\cup}(z_n) = \mathrm{Re}\Big[ &\left(\bar{\mathbf{W}}_{PP}^{-}(z_0,z_n)^H \mathbf{e}_P^M + \bar{\mathbf{W}}_{SP}^{-}(z_0,z_n)^H \mathbf{e}_S^M\right) \circ \left(\left(\partial_{c_\chi} \mathbf{R}_{PP}^{\cup}(z_n)\right) \mathbf{p}_P^{+,M}(z_n) + \left(\partial_{c_\chi} \mathbf{R}_{PS}^{\cup}(z_n)\right) \mathbf{p}_S^{+,M}(z_n)\right)^* \\ &+ \left(\bar{\mathbf{W}}_{PS}^{-}(z_0,z_n)^H \mathbf{e}_P^M + \bar{\mathbf{W}}_{SS}^{-}(z_0,z_n)^H \mathbf{e}_S^M\right) \circ \left(\left(\partial_{c_\chi} \mathbf{R}_{SP}^{\cup}(z_n)\right) \mathbf{p}_P^{+,M}(z_n) + \left(\partial_{c_\chi} \mathbf{R}_{SS}^{\cup}(z_n)\right) \mathbf{p}_S^{+,M}(z_n)\right)^* \Big],\end{aligned} \tag{A2}$$

$$\begin{aligned}\Delta \mathbf{c}_\chi^{T^-}(z_n) = \mathrm{Re}\Big[ &\left(\bar{\mathbf{W}}_{PP}^{-}(z_0,z_n)^H \mathbf{e}_P^M + \bar{\mathbf{W}}_{SP}^{-}(z_0,z_n)^H \mathbf{e}_S^M\right) \circ \left(\left(\partial_{c_\chi} \mathbf{T}_{PP}^{-}(z_n)\right) \mathbf{p}_P^{-,M}(z_n) + \left(\partial_{c_\chi} \mathbf{T}_{PS}^{-}(z_n)\right) \mathbf{p}_S^{-,M}(z_n)\right)^* \\ &+ \left(\bar{\mathbf{W}}_{PS}^{-}(z_0,z_n)^H \mathbf{e}_P^M + \bar{\mathbf{W}}_{SS}^{-}(z_0,z_n)^H \mathbf{e}_S^M\right) \circ \left(\left(\partial_{c_\chi} \mathbf{T}_{SP}^{-}(z_n)\right) \mathbf{p}_P^{-,M}(z_n) + \left(\partial_{c_\chi} \mathbf{T}_{SS}^{-}(z_n)\right) \mathbf{p}_S^{-,M}(z_n)\right)^* \Big],\end{aligned} \tag{A3}$$

$$\begin{aligned}\Delta \mathbf{c}_\chi^{R^\cap}(z_n) = \mathrm{Re}\Big[ &\left(\bar{\mathbf{W}}_{PP}^{\cup}(z_0,z_n)^H \mathbf{e}_P^M + \bar{\mathbf{W}}_{SP}^{\cup}(z_0,z_n)^H \mathbf{e}_S^M\right) \circ \left(\left(\partial_{c_\chi} \mathbf{R}_{PP}^{\cap}(z_n)\right) \mathbf{p}_P^{-,M}(z_n) + \left(\partial_{c_\chi} \mathbf{R}_{PS}^{\cap}(z_n)\right) \mathbf{p}_S^{-,M}(z_n)\right)^* \\ &+ \left(\bar{\mathbf{W}}_{PS}^{\cup}(z_0,z_n)^H \mathbf{e}_P^M + \bar{\mathbf{W}}_{SS}^{\cup}(z_0,z_n)^H \mathbf{e}_S^M\right) \circ \left(\left(\partial_{c_\chi} \mathbf{R}_{SP}^{\cap}(z_n)\right) \mathbf{p}_P^{-,M}(z_n) + \left(\partial_{c_\chi} \mathbf{R}_{SS}^{\cap}(z_n)\right) \mathbf{p}_S^{-,M}(z_n)\right)^* \Big],\end{aligned} \tag{A4}$$

$$\begin{aligned}\Delta \mathbf{c}_\chi^{T^+}(z_n) = \mathrm{Re}\Big[ &\left(\bar{\mathbf{W}}_{PP}^{\cup}(z_0,z_n)^H \mathbf{e}_P^M + \bar{\mathbf{W}}_{SP}^{\cup}(z_0,z_n)^H \mathbf{e}_S^M\right) \circ \left(\left(\partial_{c_\chi} \mathbf{T}_{PP}^{+}(z_n)\right) \mathbf{p}_P^{+,M}(z_n) + \left(\partial_{c_\chi} \mathbf{T}_{PS}^{+}(z_n)\right) \mathbf{p}_S^{+,M}(z_n)\right)^* \\ &+ \left(\bar{\mathbf{W}}_{PS}^{\cup}(z_0,z_n)^H \mathbf{e}_P^M + \bar{\mathbf{W}}_{SS}^{\cup}(z_0,z_n)^H \mathbf{e}_S^M\right) \circ \left(\left(\partial_{c_\chi} \mathbf{T}_{SP}^{+}(z_n)\right) \mathbf{p}_P^{+,M}(z_n) + \left(\partial_{c_\chi} \mathbf{T}_{SS}^{+}(z_n)\right) \mathbf{p}_S^{+,M}(z_n)\right)^* \Big],\end{aligned} \tag{A5}$$

Next, we write the recurring terms

$$\mathbf{A}_X(z_n) \approx \sum_{\kappa=0}^{K}\sum_{\lambda=0}^{\Lambda}\left(\tilde{\mathbf{A}}_X\right)_\lambda^\kappa(z_n)\,\mathbf{S}_\theta^\kappa(z_n), \tag{A6}$$

with $\mathbf{A} \in \{\mathbf{R}^\cup, \mathbf{R}^\cap, \mathbf{T}^+, \mathbf{T}^-\}$ and $X \in \{PP, PS, SP, SS\}$. Taking the derivative of $\mathbf{A}_X$ with respect to $c_\chi$ yields

$$\partial_{c_\chi}\mathbf{A}_X(z_n) \approx \sum_{\kappa=0}^{K}\sum_{\lambda=0}^{\Lambda}\left(\partial_{c_\chi}\tilde{\mathbf{A}}_X\right)_\lambda^\kappa(z_n)\,\mathbf{S}_\theta^\kappa(z_n). \tag{A7}$$

Writing out the terms $\left(\partial_{c_\chi}\tilde{\mathbf{A}}_X\right)_\lambda^\kappa$ explicitly yields

$$\left(\partial_{c_\alpha}\tilde{\mathbf{A}}_X\right)_\lambda^\kappa(z_n) = \sum_{m=0}^{\lambda}\sum_{k=0}^{\lambda-m}\frac{m}{\kappa!m!k!(\lambda-k-m)!}\left.\frac{d^{\kappa+\lambda}A_X\left(\sin(\theta),c_\alpha,c_\beta,c_\rho\right)}{d(\sin(\theta))^\kappa dc_\alpha^m dc_\beta^k dc_\rho^{(\lambda-k-m)}}\right|_{(\mathbf{0})}\mathbf{C}_\alpha^{m-1}(z_n)\,\mathbf{C}_\beta^k(z_n)\,\mathbf{C}_\rho^{(\lambda-k-m)}(z_n), \tag{A8}$$

$$\left(\partial_{c_\beta}\tilde{\mathbf{A}}_X\right)_\lambda^\kappa(z_n) = \sum_{m=0}^{\lambda}\sum_{k=0}^{\lambda-m}\frac{k}{\kappa!m!k!(\lambda-k-m)!}\left.\frac{d^{\kappa+\lambda}A_X\left(\sin(\theta),c_\alpha,c_\beta,c_\rho\right)}{d(\sin(\theta))^\kappa dc_\alpha^m dc_\beta^k dc_\rho^{(\lambda-k-m)}}\right|_{(\mathbf{0})}\mathbf{C}_\alpha^{m}(z_n)\,\mathbf{C}_\beta^{k-1}(z_n)\,\mathbf{C}_\rho^{(\lambda-k-m)}(z_n), \tag{A9}$$

$$\left(\partial_{c_\rho}\tilde{\mathbf{A}}_X\right)_\lambda^\kappa(z_n) = \sum_{m=0}^{\lambda}\sum_{k=0}^{\lambda-m}\frac{\lambda-k-m}{\kappa!m!k!(\lambda-k-m)!}\left.\frac{d^{\kappa+\lambda}A_X\left(\sin(\theta),c_\alpha,c_\beta,c_\rho\right)}{d(\sin(\theta))^\kappa dc_\alpha^m dc_\beta^k dc_\rho^{(\lambda-k-m)}}\right|_{(\mathbf{0})}\mathbf{C}_\alpha^{m}(z_n)\,\mathbf{C}_\beta^{k}(z_n)\,\mathbf{C}_\rho^{(\lambda-k-m-1)}(z_n). \tag{A10}$$

Once again, while these terms are difficult to evaluate by hand, they can be straightforwardly evaluated using mathematical software such as Maple.